

This is the peer reviewed version of the following article:

Experimental and numerical study on the adoption of split injection strategies to improve air-butanol mixture formation in a DISI optical engine / Breda, S.; D'Orrico, F.; Berni, F.; d'Adamo, A.; Fontanesi, S.; Irimescu, A.; Merola, S. S.. - In: FUEL. - ISSN 0016-2361. - 243:(2019), pp. 104-124. [10.1016/j.fuel.2019.01.111]

Terms of use:

The terms and conditions for the reuse of this version of the manuscript are specified in the publishing policy. For all terms of use and more information see the publisher's website.

11/01/2025 21:11

Experimental and Numerical Study on the Adoption of Split Injection Strategies to Improve Air-Butanol Mixture Formation in a DISI Optical Engine

S. Breda^{1*}, F. D'Orrico¹

F. Berni², A. d'Adamo², S. Fontanesi²

A. Irimescu³, S. S. Merola³

¹*R&D CFD S.R.L, Modena, Italy*

²*Department of Engineering "Enzo Ferrari," University of Modena and Reggio Emilia, Modena, Italy*

³*Istituto Motori - CNR, Napoli, Italy*

(*) corresponding author: sebastiano.breda@red-cfd.it

Abstract

Gasoline replacement with alternative non-fossil fuels compatible with existing units is widely promoted around the world to reduce the dependency on oil-based products by adopting domestic renewable sources. In this context, the possibility to obtain bio-alcohols from non-edible residues of food and plants is particularly attractive for gasoline replacement in SI (Spark Ignition) engines. Such bio-fuels are characterized by higher laminar flame speed (LFS) and octane rating, resulting in improved thermal efficiency and reduced regulated emissions. Low-carbon alcohols (e.g. ethanol) are disadvantageous as gasoline replacement due to poor energy density and high corrosive action on distribution pipelines, whereas high-carbon ones (e.g. n-butanol) are particularly promising candidates thanks to the physical properties and the energy density closer to those of gasoline. High latent heat of vaporization and low saturation pressure are the most relevant weaknesses of n-butanol related to gasoline replacement in DISI (Direct Injection SI) power units. On equal injection pressure and phasing, the slow evaporation rate of n-butanol leads to poor mixture preparation and larger fuel deposits. In particular, this is emphasized by low charge and wall temperatures during part load operation, reducing combustion efficiency and promoting the formation of pollutant particles.

Split injection is a promising strategy to improve charge preparation contemporary reducing fuel deposits and improving mixture homogeneity, mostly for low-evaporating fuels. In the present work different split injection strategies are tested in an optically accessible SI engine fueled with n-butanol and simulated through CFD with the aim of identifying trends and understanding the root causes behind measured behaviors. CFD simulations help in understanding changes in charge stratification using different injection strategies, allowing to explain both combustion behavior and soot formation tendency from the analysis of fuel distribution. Mixture quality in the spark region and the presence of very rich mixture pockets in the combustion chamber are identified as the most critical aspects that should be optimized when changing the injection strategy; this in turn contributes to avoid slow burn rates or excessive soot production during operation with low evaporating fuels such as n-butanol. A strong correlation between diffusive flames and rich mixture pockets is found in terms of both location and intensity, proving the first order role of fuel deposits formation and mixture homogenization on both combustion development and soot formation.

Keywords

Spark ignition engine, direct injection, butanol, split injection strategy, CFD simulation

1.Introduction

1.1 Background

Emission reduction represents one of the key tasks in the recent internal combustion engine development. Since the last two decades, the automotive sector has been characterized by progressive limitation for tailpipe emissions and increasing efficiency targets, both a consequence of a broader and international political strategy aiming at a new low-carbon economy (LCE) [1,2]. Such constraints apply to both conventional fossil fuels and ones produced from renewable sources. Both global warming and medium-term oil availability are fundamental justifications for LCE implementation. In addition to this, the oil price rise is becoming more and more critical approaching to the raw material complete depletion condition.

Focusing on SI engine development, in the last years it has become clear that a re-thinking of the whole combustion process design is mandatory to obtain goals hardly attainable with the addition of after-treatment devices only. In this scenario the replacement of gasoline with alternative non-fossil derived fuels (biofuels) represents the most promising and interesting way to achieve the LCE goal.

Biofuels can be produced from biomass, which is a 100% renewable, carbon neutral and relatively abundant source: it is estimated to be the fourth largest source of primary energy in the world, able to cover approximately 12-14% of the global energy consumption [3]. According to different biomass conversion techniques, it is possible to distinguish between first and second biofuel generation [4]. First generation biofuels are obtained through edible biomass conversion using biochemical processes: this represents a troublesome dispute for biofuel diffusion, because of the competition with food, fibre and biomaterial production. Second generation biofuels overcome this issue, as they can be obtained through thermochemical processes (like pyrolysis) using non-edible biomass, such as municipal solid waste, agricultural wastes, industrial organic residues and human and animal wastes [5-6].

Amongst all the available biofuels, bio-alcohols represent the best choice as gasoline substitutes because of their chemical and physical properties. The high octane rating and flame speed of bio-alcohols lead to higher thermal efficiency and to generally lower regulated emissions [7- 10]. The main physical properties of gasoline and bio-alcohols are resumed in Table 1.

Table 1: Alcohols and Gasoline main properties from [4,11]

Fuel	Gasoline	Methanol	Ethanol	n-Butanol
Molecular Formula	C ₄ -C ₁₂	CH ₃ OH	C ₂ H ₅ OH	C ₄ H ₉ OH
Lower Heating Value [MJ/kg]	42.9	20.08	26.83	32.01
Density @ 20 °C [kg/m ³]	744.6	791.3	789.4	810
Research Octane Number [-] RON	92	111	108	96
Motor Octane Number [-] MON	82	88.6	90	78
Latent Heat of Vaporization [kJ/kg]	373	1098	838	584
Self-Ignition Temperature (°C)	300	470	474	385
Stoichiometric Air-to-Fuel Ratio	14.7	6.43	8.94	11.12

Compared to gasoline the main drawbacks of alcohols are the lower air-to-fuel stoichiometric ratio (AFR) and the lower energy density, both responsible of a greater fuel consumption on equal engine output. When choosing the alcohol-fuel, the carbon concentration represents one of the key characteristics to be taken into account : high-carbon content means higher heating value. This shifts the interest from low-carbon to high-carbon alcohols. Low-carbon alcohols (e.g. ethanol or methanol) have been long analysed because of their appealing knock resistance and emission levels compared to high-carbon alcohols. However, low energy content, fuel consumption and marked corrosive action on distribution pipelines prevent the complete replacement of gasoline with such bio-alcohols. On the contrary, high-carbon alcohols (e.g. butanol) reduce the corrosive action and they have energy density comparable to gasoline: hence they represent a better trade-off to reduce the dependency on fossil fuels and to substitute gasoline in existing units without massive engine design modifications [4,12].

The butanol molecule has four structural isomers, determining different thermodynamic properties and combustion characteristics [13]. In Table 2 the physical properties of n-butanol, sec-butanol, tert-butanol and iso-butanol are listed. Sec-butanol has an excessively low MON octane number to be considered as a possible gasoline substitute and tert-butanol use is limited to low volumetric fraction due to the high melting point. Iso-butanol is the isomer ensuring the highest knock resistance in SI engines, thanks to the highest RON and MON. Finally, n-butanol has physical properties more similar to gasoline than other isomers, thanks to the straight-chain structure. Therefore, this last is the most promising candidate for gasoline substitution.

Table 2: Chemical Structures and physical properties of butanol isomers [13].

Property	n-Butanol	iso-Butanol	sec-Butanol	tert-Butanol
Boiling Point/°C	117.7	108	99.5	82.4
Density/kg-m ⁻³	809.8	801.8	806.3	788.7
Research octane number (RON)	96	113	101	105
Motor octane number (MON)	78	94	32	89
Enthalpy of vaporization at T _{boil} kJ/kg	582	566	551	527
Viscosity at 25 °C/MPa s	2.544	4.312	3.096	/

According to the properties listed in Tables 1 and 2, n-butanol should in principle ensure the highest thermal efficiency, due to a faster and complete combustion process (highest LFS), with similar fuel consumption and power output compared to gasoline. The main drawback is represented by the low volatility that could lead to poor mixture preparation and fuel deposit formation in DI engines, reducing combustion efficiency.

Pure and gasoline blended n-butanol combustion was studied by Szwaja and Naber [12] in a PFI variable compression ratio engine at 900 rpm at both part and full load conditions. n-Butanol showed an advanced combustion phasing (MFB-50%) due to a shorter early burn duration and a similar overall duration, with a slightly increased stability compared to gasoline at part load, measured through the Coefficient of Variation (COV) of the indicated mean effective pressure (IMEP), COV_{IMEP}. Rate and duration of combustion were similar also using butanol-gasoline blends, demonstrating the suitability of n-butanol as gasoline substitute as neat or blended fuel. Similar results were obtained by Aleiferis et al., who compared in [14] the combustion and flame development in a DISI engine using ethanol, butanol, gasoline and iso-octane. At stoichiometric and lean conditions, ethanol always showed the fastest burn rate compared to all the other fuels, while a similar behaviour between gasoline and butanol was generally measured. A higher sensitivity of combustion to the coolant temperature was measured using butanol, behaving similarly to gasoline for low coolant temperature and similarly to ethanol for higher coolant temperature (from 20°C to 90°C) at stoichiometry; as for lean mixtures (from $\Phi=1$ to $\Phi=0.83$) butanol burn rate was always higher than gasoline one. The higher sensitivity to coolant temperature using butanol suggests that a higher sensitivity to mixture formation can be experienced when replacing hydrocarbons with alcohols in DI engines, overcoming the benefit of higher LFS. The same authors in [15] studied fuel deposit formation with the same fuels through images and heat flux measurements, showing one order of magnitude difference in the heat fluxes when substituting gasoline with ethanol or butanol at both firing and motored conditions. The authors motivated such evidence by addressing spray-wall interaction. Split injection strategies were found to be effective in reducing spray impingement through spray penetration shortening. The fuel film surviving throughout the engine cycle in firing conditions when using gasoline could be eliminated using triple injection: this did not happen using ethanol and butanol if the coolant temperature was 20°C or 50°C respectively (confirming the higher tendency of butanol to produce wall film compared to ethanol), but a strong improvement was still observed comparing the split injection strategy with the single one. As for this last, a surviving fuel wall film was always measured, except for the 90°C coolant temperature case.

The potential substitution of gasoline with n-butanol was tested by the authors for different loads and global mixture qualities in an optically accessible DISI engine in [11,16]. Different outcomes were found at both part-load and WOT (Wide Open Throttled) operations using stoichiometric and lean global mixtures in terms of combustion phasing and duration [17]. A longer 0 to 10% of mass fraction burned (MFB) and a delayed MFB 50% were measured fuelling the engine with n-butanol compared to gasoline when using the same spark time and injection strategy, leading to an increase in COV_{IMEP} during lean WOT operation ($\Phi=0.75$). Three-dimensional CFD analyses pointed out as root causes for the experimental evidence the poor mixture preparation in terms of charge homogeneity and the different crevices filling mechanism. Both these aspects were consequence of the low volatility and reduced saturation pressure of n-butanol compared to gasoline. Advanced and delayed injection strategies (with respect to the gasoline optimized baseline) were also tested at different

engine operations using butanol and gasoline, monitoring engine output and emissions formation. Minor variations were measured by changing the injection phasing in terms of engine output and combustion stability using gasoline, while a strong impact of injection phasing was found using n-butanol. A reduction of power output and a considerable increase in COV_{IMEP} was recorded when retarding the n-butanol injection; a high sensitivity to charge stratification was then confirmed by CFD analyses [17,18].

1.2 Current Analysis

Previous studies showed a higher dependency of both engine output and emissions formation on the injection strategy in DISI engines fuelled with alcohols, compared to those using gasoline. This suggests that different control strategies should be implemented when replacing gasoline with butanol, accounting for the optimization of jet penetration to reduce wall impingement, improve mixture homogeneity and suppress particulate emissions [19]. The purpose of the current analysis is the evaluation of the impact of alternative injection strategies on performance and engine-out emissions at part load. Starting from the optimized start of injection (SOI) for single-pulse fuel delivery, different split injection strategies are both tested in an optically accessible research engine fuelled with n-butanol under fixed spark timing and simulated through 3D-CFD. Simulation results allow to further validate the CFD methodology on experimental measurements and to understand the root causes behind combustion development and soot formation variations when changing the injection strategy.

2.Methods

2.1 Engine Characteristics and Operative Conditions

Experimental investigations were performed on an optically accessible single cylinder DISI engine. It is equipped with the cylinder head of a commercial SI power unit, with four valves per cylinder and a centrally located spark plug. The fuel system features a side-mounted six-hole solenoid injector in a wall-guided configuration. The exact orientation of the 6 spray plumes is reported in Figure 1 as well as the angles between the relative axes, as set-up in the engine head (Table 3). Due to the wall guided architecture of the commercial engine head, 5 of the 6 plumes target the piston (one of them is almost vertical), while the last one has an axis parallel to the injector one. Such hole orientation was originally optimized to guarantee an improved mixture quality in the spark region during stratified charge operation, thanks to the presence of a bowl shaped piston. In the current application the original piston is replaced by a transparent flat one, to ensure optical access to the combustion chamber, and only homogenous charge conditions were considered, similar to how most production DISI units are run.

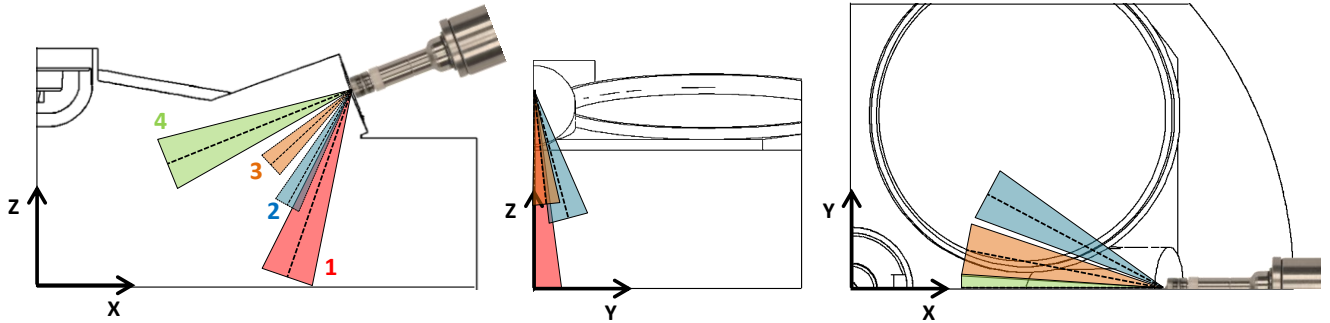


Figure 1: Schematic representation of spray plumes orientation.

Table 3: Injector hole axes orientation.

	Hole 1	Hole 2	Hole 3	Hole 4
Angle xy (°deg)	180	207.23	190.92	180
Angle xz (°deg)	109.2	119.4	131.6	158.3
Angle yz (°deg)	90.0	80.55	86.06	90.0

A conventional Bowditch design [20] was used for optical accessibility, with a transparent crown (18 mm thick fused-silica window, which ensured a field of view 63 mm in diameter), which was screwed onto the piston. Therefore, the combustion chamber was visible through a UV-enhanced 45-degree mirror, mounted within the hollow piston. Further details on the experimental apparatus are shown in Figure 2.

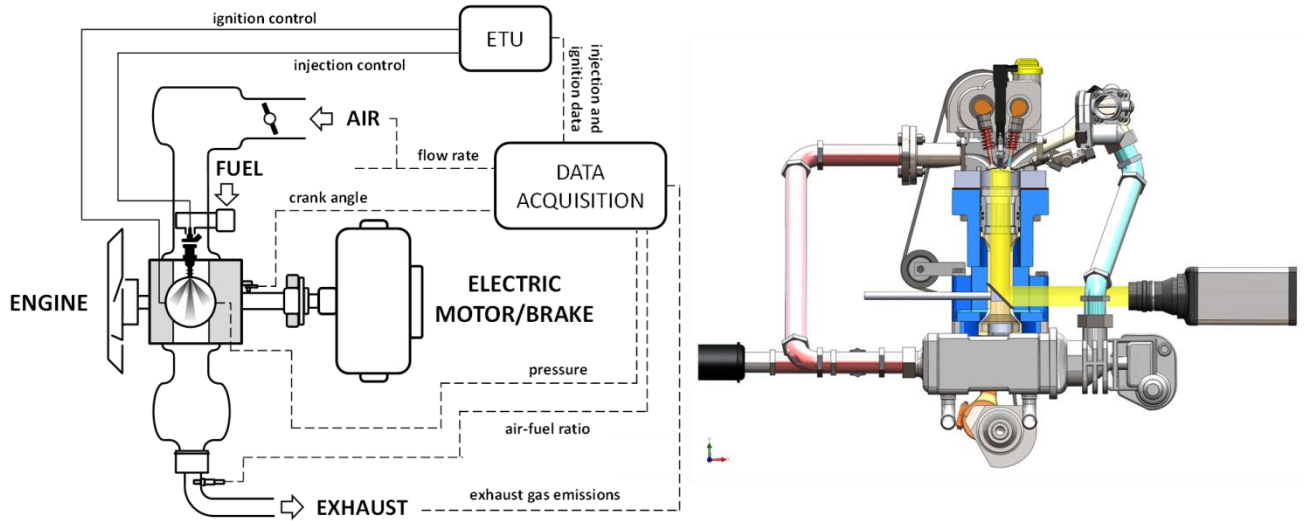


Figure 2: Schematic representation of the experimental setup and optical accessibility

The engine featured self-lubricating bronze-Teflon piston rings required for preventing fouling of the window with oil droplets, even though (along with tolerance limits specific for optical units) it also resulted in non-negligible blow-by during both the compression and the power strokes. Considering the 40 mm distance between the first ring and the upper-most surface of the piston crown, a relatively high crevice volume was present as well, with the top-land region as the major contributor. The main geometrical engine characteristics are reported in Table 4 (with CAD for crank angle degrees, TDC for top dead centre and b/a for before/after).

Table 4: Engine characteristics and operative conditions

Bore x Stroke	79 x 81.3 mm
Connecting rod length	143 mm
Cylinder	1
Compression ratio	10
IVO	3 CAD bTDC
IVC	36 CAD aBDC
EVO	27 CAD bBDC
EVC	0 CAD aTDC
Fuel system	direct injection 100 bar

In the current study a variation of the injection strategy when using n-butanol as fuel was studied at fixed engine speed, load and spark advance, with the aim of isolating fuel stratification effects. Crank shaft rotational velocity was set at 2000 rpm, intake pressure at 0.7 bar and spark timing at 30 CAD bTDC. The same total fuel quantity was injected in the split-injection cases: the injection was subdivided in two events, with a constant start of injection (SOI) of the first pulse (named SOI_1) at 300 CAD bTDC in all the cases that were investigated. Two different sensitivity analyses were carried out:

- Firstly the relative duration of the two injection pulses (i.e. the injected mass per pulse) was varied while retaining the same delta time between the start of the first and of the second injection pulses (SOI_2 - SOI_1) equal to 100 CAD. The total injection duration of 32 CAD was divided in two portions with a relative weight of 70%-30%, 50%-50% and 30%-70% as schematized in Figure 3 (a), injecting a higher mass portion during the initial/final part of the intake stroke.

- Secondly a sensitivity analysis to the phasing of the second pulse was carried out for the 50%-50% case, delaying or advancing by 50 CAD the start of the second injection SOI_2 with respect to the 100 CAD dwell time case. This is schematized in Figure 3 (b).

The phasing and duration of the tested injection strategies are resumed in Table 5.

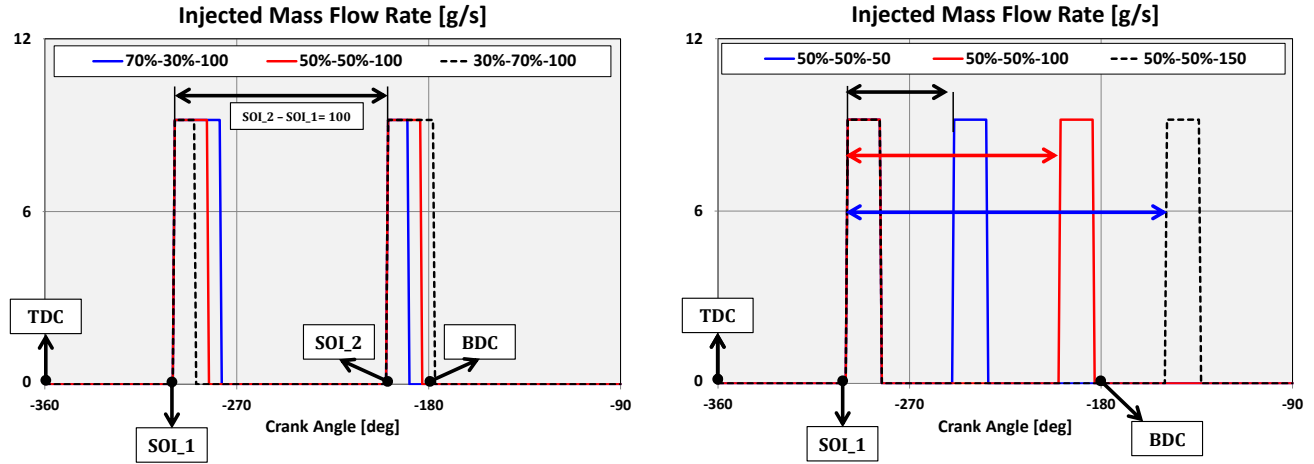


Figure 3: Injected mass flow rate in tested injection strategies changing the relative duration of the two injection pulses (a, left) and the phasing of the second injection pulse (b, right).

Table 5: Resume of tested operating conditions

Case Name	SOI_1	SOI_2	DURATION_1	DURATION_2
70%-30%-100	300 CAD bTDC	200 CAD bTDC	22 CAD	10 CAD
50%-50%-100	300 CAD bTDC	200 CAD bTDC	16 CAD	16 CAD
30%-70%-100	300 CAD bTDC	200 CAD bTDC	10 CAD	22 CAD
50%-50%-50	300 CAD bTDC	250 CAD bTDC	16 CAD	16 CAD
50%-50%-150	300 CAD bTDC	150 CAD bTDC	16 CAD	16 CAD

2.2 Experimental Methodology

The engine head was equipped with a flush-installed piezo-electric transducer (AVL GH12D) for in-cylinder pressure measurements with crank angle resolution of 0.2 CAD and an accuracy of $\pm 1\%$. In this work, indicated pressure signals of 200 consecutive cycles (without skip firing) were recorded for each operating condition. Based on these average traces, MFB values were calculated using a simplified first law analysis [16] to evaluate the 0-10% MFB and 0-50% MFB combustion durations. Other parameters such as intake pressure, air, coolant and lubricant temperatures were similarly determined. Coolant temperature was set at 325 K to allow longer combustion runs without risking piston thermal expansion close to the tolerance limit; in this way, the investigated working conditions were closer to steady-state situations usually found in real-world applications.

Air-fuel ratio was monitored with an accuracy of $\pm 1\%$ through measurements with a wide band oxygen gas sensor fitted at the exhaust. Exhaust gas concentrations of pollutant species were determined using a gas analyser based on the nondispersive infrared (NDIR) measurement principle for carbon monoxide (CO) and unburned hydrocarbons (n-hexane equivalent HC); the electrochemical method was employed for nitrogen oxide (NO_x) emissions. Accuracy was within 3%,

and the resolution of the readings for the first component was 0.01% and 1 ppm for the other two species. Opacity measurements were performed using the light absorption method, with an accuracy of 3% and a resolution of 0.1%.

Optical investigations for the analysis of combustion processes and liquid fuel film oxidation were performed by using a CMOS high-speed camera (Optronis CamRecord 5000) that ensured good sensitivity in the visible wavelength range (9V/lux second at 550 nm). The detector was coupled with 50-mm focus Nikon lens (f/1.8D) and worked in full chip configuration (512x512 pixel), with an acquisition speed of 5000 fps and an exposure time of 200 μ s. The f/stop of the lens was fixed at 2.8; in this way, the optical set-up gave a resolution of 188 μ m per pixel, with a signal to noise ratio sufficient to apply image processing for the analysis of the flame front propagation even during the early stages of combustion. Digital image sequences related to each engine operative condition consisted in 240 CADs per cycle after spark timing, during 30 consecutive engine cycles. Synchronization of various control triggers for ignition, injection and camera was achieved using the optical encoder mounted on the crankshaft as an external clock connected to an AVL Engine Timing Unit.

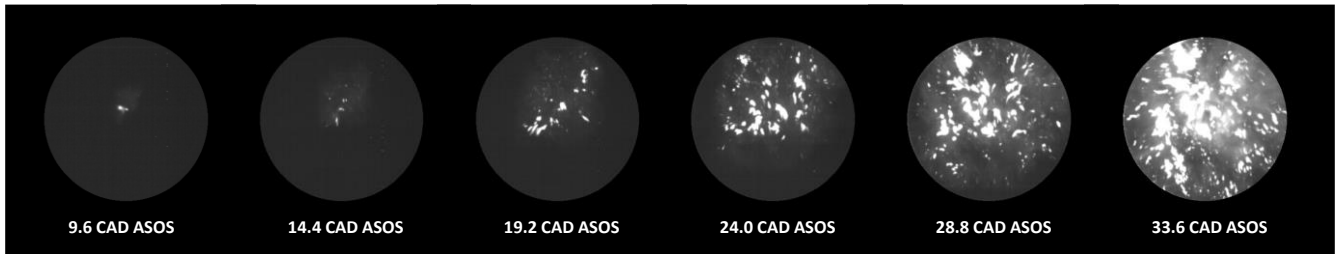


Figure 4: Flame images recorded during the engine cycle closest to the average pressure trace for the single injection strategy.

Figure 4 shows selected images (ASOS stands for after start of spark) recorded during the cycle that featured a pressure trace closest to the average one in the case of single injection (SOI_300 CAD bTDC). As observed in previous experiments on the same optical device [11,16,19], flames initiated from the spark and generally featured a preferred direction of propagation towards the exhaust valves. This was due to the combined effect of higher wall temperatures in that region of the combustion chamber, tumble motion and charge stratification [19,21].

The bright spots in the burned gas enclosed by the “normal” flame front were due to oxidation of fuel-rich regions determined by the impingement of fuel jets on the piston surface; this induced diffusive flames that persisted in the late combustion phase. The emission intensity and spatial distribution of these flames were strongly dependent on injection timing, as shown in Figure 5.

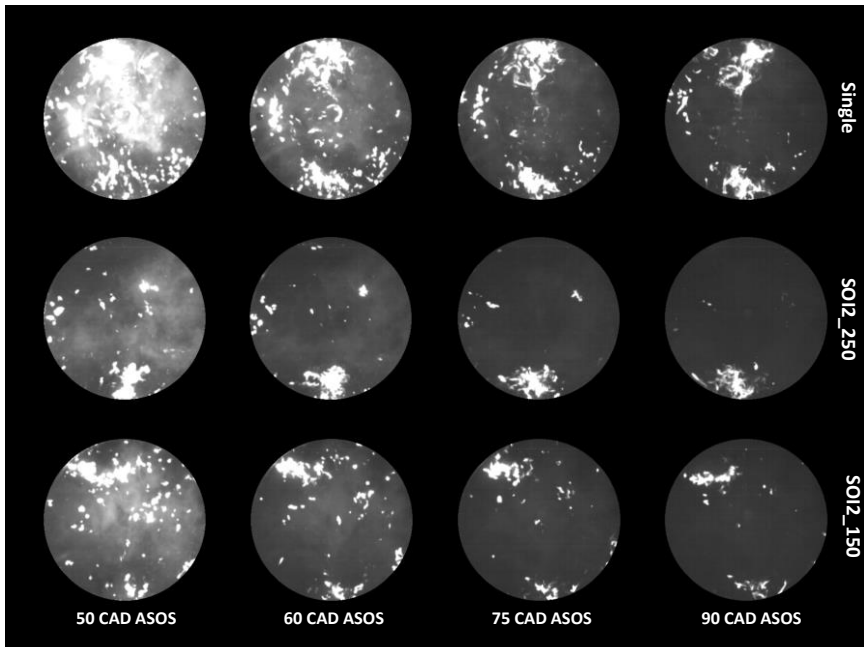


Figure 5: Flame images recorded in the late combustion stages, during the engine cycle closest to the average pressure trace.

In a previous work and with gasoline fuelling, two types of diffusive flames were identified [22]: the first was associated to the oxidation at the gas-liquid interface and the second to “jet-like” flames associated to unburned gas backflow from the top-land region [21,23]. For this study, the evidence of flames originating from the top-land region was negligible, while the first type of diffusive oxidation occurred for all the investigated conditions. In particular, flames close to the intake side, originated by fuel jets impinging on the piston crown, were found to be easily detectable. The effect was determined by the specific orientation of one of the six jets that was almost vertical and induced liquid film formation repeatedly on the same region of the piston surface; the two other jets closer to the aforementioned one most likely contributed to this phenomenon, more prominent as the injector-piston distance was lower.

In order to obtain quantitative results on the spatial distribution and time evolution of diffusive flames with an adequate statistical approach, all detected image sequences were treated by Vision Assistant of National Instruments, applying an image processing procedure previously developed and optimised [19,22,24]. The fundamental steps of the procedure are sketched in Figure 6. Specifically, after applying a circular mask to the 256-grey scale images (Figure 6, left), a power look-up table (LUT) function was applied (with constant 1.5) to increase the contrast in bright regions (Figure 6, middle). This step highlighted the diffusive flames with respect to the luminosity induced by the spark ignited burned gas. The binary images were obtained by applying a 30% luminosity threshold (Figure 6, right). Finally, the coordinates of the luminous centroids related to the detected diffusive flames at fixed crank angle after spark timing (60 CDA ASOS) were accumulated for 30 consecutive acquisitions and results were represented as histograms. For each fuel injection strategy, the most probable spatial distribution of diffusive flames was obtained by considering the grinding method of Kriging [18,25] and represented by using Surfer v.11 by Golden Software.

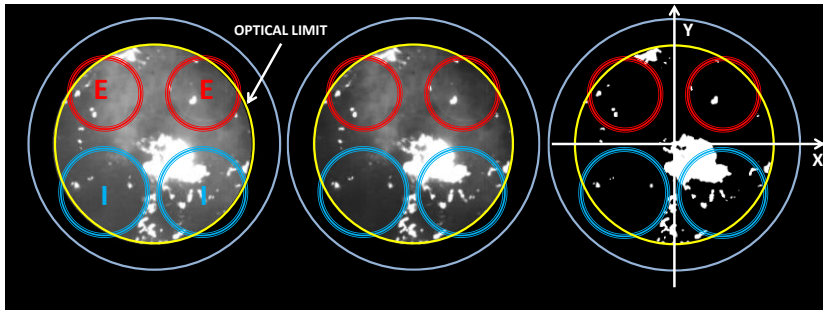


Figure 6: Sketch of the image processing steps for the analysis of diffusive flames induced by liquid fuel film presence on the piston crown.

2.3 CFD Methodology

The CFD analyses are carried out through the commercial code STAR-CD version 4.28.033, licensed by SIEMENS PLM. The 3D-CFD model covers half of the combustion chamber and one of the two intake and exhaust ports, due to the symmetry of the fluid domain. The spark plug geometry is fully retained in the model, as well as the crevice between the piston crown, the liner and the first ring. Pressure and temperature time-varying boundary conditions are applied at both intake and exhaust ports and they are derived from a tuned 1D model of the whole experimental apparatus. A mass flow rate boundary condition is applied in the crevice bottom accounting for the measured blow-by leakage [17]. The average size of the computational in-cylinder and ports mesh is 0.7 mm, leading to a 1.2 and 0.4 million cells at BDC/TDC respectively, while in the crevice volume (0.5 mm thickness) the mesh size is 0.1 mm. A picture of the computational domain and of the numerical grid is reported in Figure 7. The computational time for the simulation of one engine cycle is about 72 hours on 32 CPUs. The most significant sub-models (and model constants) adopted for the simulations are listed for completeness in Appendix 1 and hereafter briefly recapped. CFD analyses are carried out in a RANS framework using the $k-\epsilon$ RNG turbulence model, region-specific wall temperatures and the GruMo-UniMORE wall heat transfer model to take into account heat transfer at the combustion chamber walls [26,27].

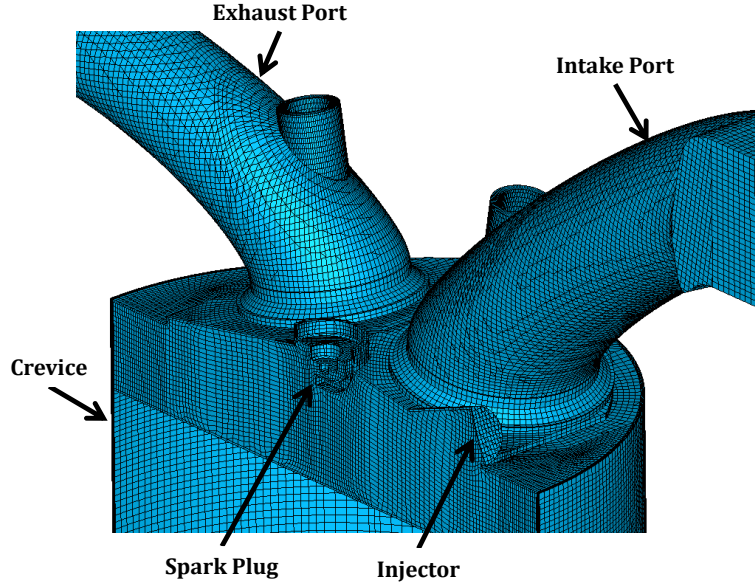


Figure 7: Sketch of the computational domain and grid.

An accurate prediction of the fuel stratification before combustion onset is a crucial aspect for the CFD evaluation of both combustion velocity and emission formation. An established methodology for each of the fuel properties, for the spray characteristics and for the spray-wall interaction [17,28,29] is used to simulate both the full-cone GDI spray evolution and the interaction of the liquid phase with the solid walls. Butanol spray is simulated through the injection of Lagrangian particles replacing the primary break-up with a Rosin-Rammler distribution calibrated on experimental measurements in a quiescent vessel [30]. Starting from nominal nozzle length and diameter (0.140 and 0.196 mm, respectively) the effective nozzle area is estimated using the Kuensberg 1-D model [31], while the droplet initial velocity is calculated through the prescribed experimental mass flow rate. The spray simulation is validated against experiments carried out in a spray bomb using different fuels (gasoline and butanol) and injection pressures (50 and 100 bar) [17,32,33]. The mass flow rate unbalance between the 6 nozzles is accounted for using nozzle-specific discharge coefficients, in order to simultaneously reproduce spray penetration, droplet diameter and global spray morphology.

Spray-wall interaction is governed by wall temperature and roughness, droplet velocity, diameter and relative impact angle, as well as fuel physical properties. A consistent simulation of fuel deposit formation can only be obtained accounting for all these aspects, in particular the non-dimensional temperature T^* that according to Rosa [34] is the key parameter to distinguish different impact regimes (nucleate, transition and film boiling). T^* is a function of the Nukiyama, Leidenfrost and wall temperatures (T_N , T_L , T_W respectively) as in Equation 1. Droplet deposition is allowed only if the non-dimensional temperature T^* is lower than 1, while increasing the wall temperature ($T^* > 1$) droplet deposition does not occur, due to the formation of a thin vapor layer between the heated wall and the impacting droplet.

$$T^* = \frac{T_W - T_N}{T_L - T_N} \quad (\text{Equation 1})$$

In absence of experimental measurements for Nukiyama and Leidenfrost temperatures, these are estimated using the Habchi model [35], considering the thermodynamic properties of the liquid such as boiling, critical and saturation temperatures [28]. The ECFM-3Z combustion model [36] is used for the prediction of the turbulent flame development, thanks to the capability to model partially-premixed combustion events. It is coupled to a simple algebraic model accounting for spark ignition and early flame kernel formation [37]. The combustion model is based on the flame surface density (FSD) concept, considering the laminar flame velocity (property of the air/fuel local mixture), that is an input for the model itself, and accounting for the wrinkling effect of turbulence on the flame according to the “flamelet hypothesis”, from which a turbulent flame propagation is calculated. In the adopted commercial code, the required correlation expressing the laminar flame speed (LFS) of the specific fuel tested as a function of pressure, temperature and mixture quality is not available, as for other unconventional fuels for both SI and CI engines. To overcome this modeling issue an in-house developed

methodology [17,39,40], hereafter summarized, is used to define a polynomial function expressing the n-butanol LFS at engine conditions.

As first step the fuel specific LFS is calculated through detailed chemistry simulations over a wide range of engine-like pressure and temperature conditions using the chemistry solver DARS v4.02 and the validated Frassoldati et al. chemical mechanism [38]. Moving from the assumption that the dependency of LFS on pressure, temperature and mixture quality can be expressed by the quite common power law in Equation 2, in which the laminar flame speed LFS is a function of pressure temperature and three coefficients (T , p , LFS_0 , α and β respectively), an accurate form for LFS_0 , α and β as a function of the equivalence ratio Φ is derived via fitting the complex chemistry calculated population.

$$LFS = LFS_0 \cdot \left(\frac{T}{T_0}\right)^\alpha \cdot \left(\frac{p}{p_0}\right)^\beta \quad (\text{Equation 2})$$

The results of the fitting procedure, whose details can be found in [17], are 18 coefficients (a_i , b_i , c_i , reported in Appendix 2) which are placed in the summations in Equation 3, and allow to calculate the LFS of the specific fuel for any given value of pressure, temperature and equivalence ratio.

$$LFS = \left[\sum_{i=0}^5 a_i \cdot \log(\Phi)^i \right] \cdot \left(\frac{T}{T_0}\right)^{\sum_{i=0}^5 b_i \cdot \log(\Phi)^i} \cdot \left(\frac{p}{p_0}\right)^{\sum_{i=0}^5 c_i \cdot \log(\Phi)^i} \quad (\text{Equation 3})$$

The obtained polynomial form is used as an input for the combustion model, thus overcoming uncertainties related with LFS prediction at engine-like conditions using alternative fuels. A comparison between the chemistry-based LFS of gasoline and n-butanol at different conditions is reported in Figure 8: as expected, n-butanol shows higher LFS than gasoline under the same pressure, temperature and AFR.

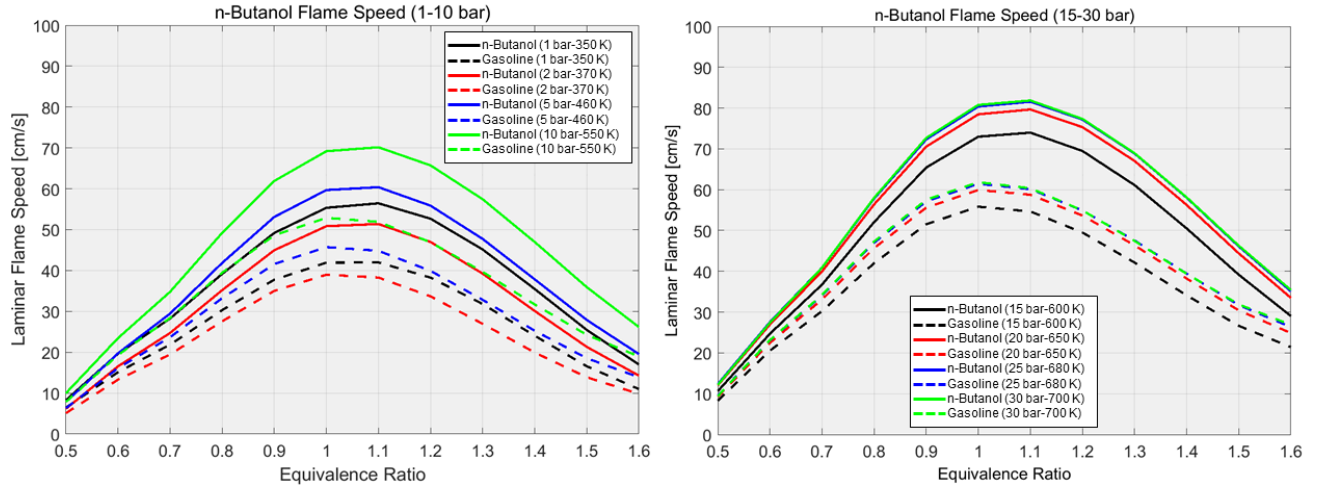


Figure 8: Comparison between the calculated Laminar Flame Speeds (LFS) of n-butanol and Gasoline at engine-like pressure and temperature conditions as a function of the mixture equivalence ratio (EGR=0%).

No complex model are used for the prediction of soot in the 3D CFD simulations. However, a purely chemical kinetics study is carried out aiming at correlating charge stratification and soot production: such approach is used to evaluate which are the temperature and mixture quality conditions promoting soot formation/oxidation using n-butanol. The general goal is to propose a CFD methodology to evaluate the performance of different injection strategies in terms of soot tendency, thus avoiding the increase in computational effort related to the calibration of complex soot models while retaining a high degree of chemistry fidelity. Equivalence Ratio (ER)/Temperature maps of the rate of production of Polycyclic Aromatic Hydrocarbons (PAH, i.e. the most relevant soot precursors) and of the soot oxidation rate are built using a validated reduced chemical kinetic mechanism [41,42]. This includes 76 chemical species and 349 reactions, and a 1D flamelet approach is used to simulate the range of interest in terms of temperature and equivalence ratio. In the resulting maps, reported in Figure 9, the PAH soot precursor species shows a maximum rate of formation for ER values higher than 2 and for temperatures in the range 600 K- 1200 K, while oxidation processes are promoted for ER lower than 1 and temperatures higher than 1600 K.

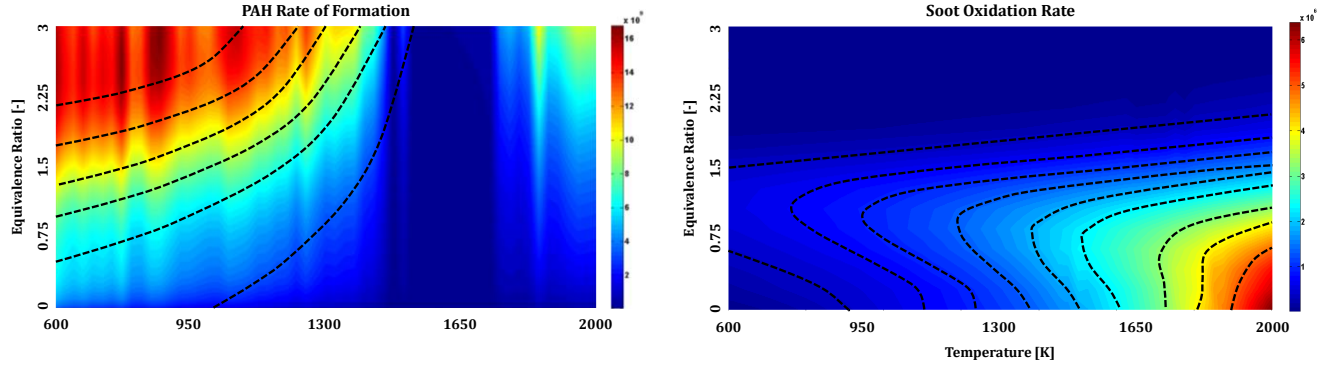


Figure 9: Equivalence Ratio/Temperature Maps of PAH formation rate (left) and oxidation rate (right) from detailed chemistry from [18].

3. Results and Discussion

3.1 Overall Experimental Results

Three different split injection strategies were tested in the optical engine by changing the relative duration of the two injection pulses, as schematized in Figure 3 (left) and resumed in Table 5. The total injection duration is constant in all the cases and equal to the single injection one (i.e. same injected mass), resulting in a very similar global AFR. The overall IMEP is reported in Figure 10, along with the IMEP coefficient of variation that is generally slightly improved (i.e. lower CoV) when adopting split injection strategies. However, despite the same spark timing, large differences between the three cases are found in terms of combustion duration, resulting in non-negligible variations in terms of in-cylinder pressure peak.

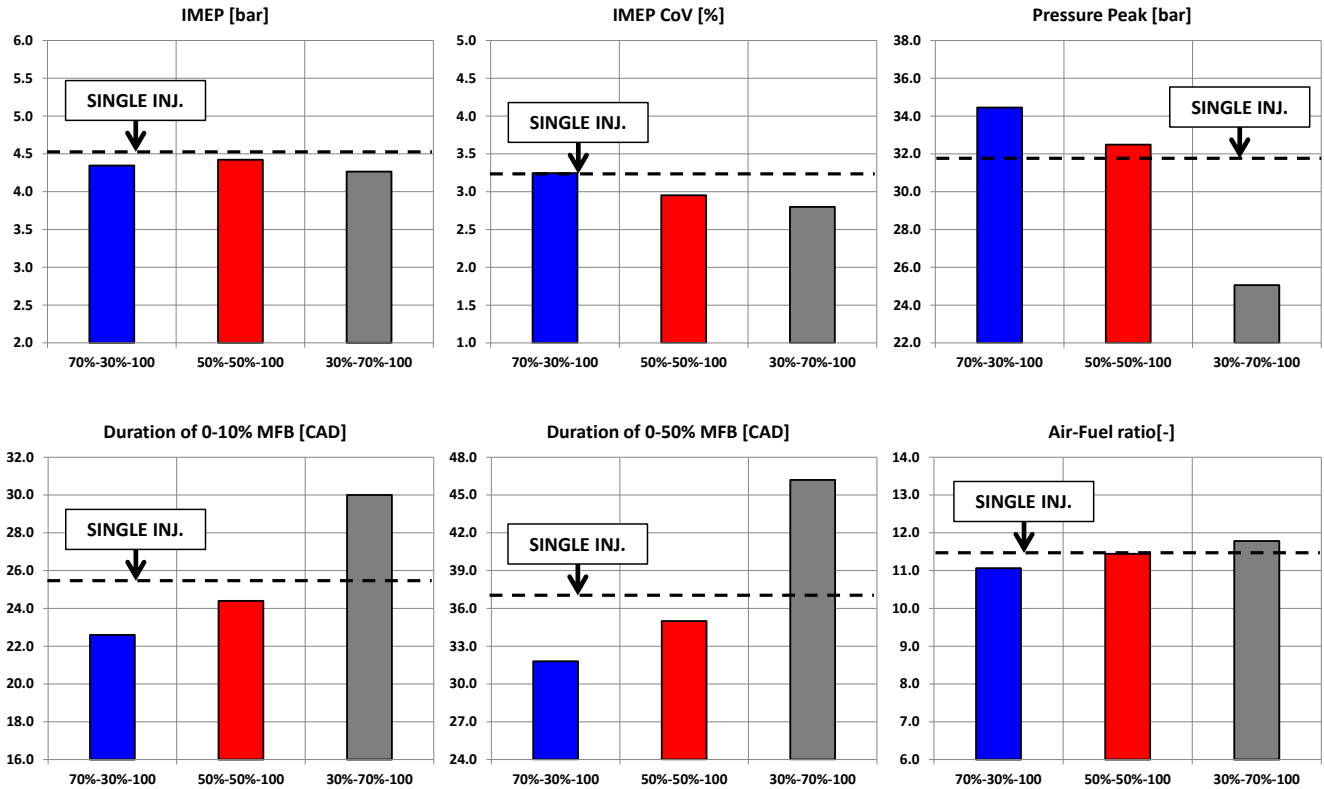


Figure 10: Overall engine output performance at different relative durations of the two injection pulses.

The general trend is a shortening of both 0-10% and 0-50% MFB when reducing the second injection pulse duration (i.e. fast burn rate). An improvement of both early and main combustion duration with respect to the single injection strategy is

in fact measured in the 70%-30% and 50%-50% cases, while a strong combustion phasing delay is measured in the 30%-70% case. Despite the trend of increasing combustion phasing/duration for longer second injection pulses, an improvement in combustion stability was measured (i.e. a decrease in $IMEP_{COV}$). This result suggests that the late injection of a large amount of fuel leads to a more repeatable, though less homogeneous, mixture formation inducing slower but more repeatable flame propagation.

The same conclusions are drawn analyzing the effect on combustion variability, when changing the second injection pulse timing, in the 50%-50% split injection strategy. Figure 11 shows a reduction of combustion variability when moving the second injection pulse towards the compression stroke. A generally lower variability of combustion duration, IMEP and pressure peak are found with a slight increase of combustion duration for both anticipated and delayed second pulses with respect to the reference 50%-50% strategy (50%-50%-100). This is probably related to a different charge stratification in the spark plug region, responsible for an increased duration of the early combustion phase. It is important to underline that the “best” tested split injection strategy (50%-50%-150) shows a 0.8% improvement of $IMEP_{COV}$ with respect to the single injection case, thus confirming the benefit of an optimized injection strategy in DI units fueled with low-evaporating fuels.

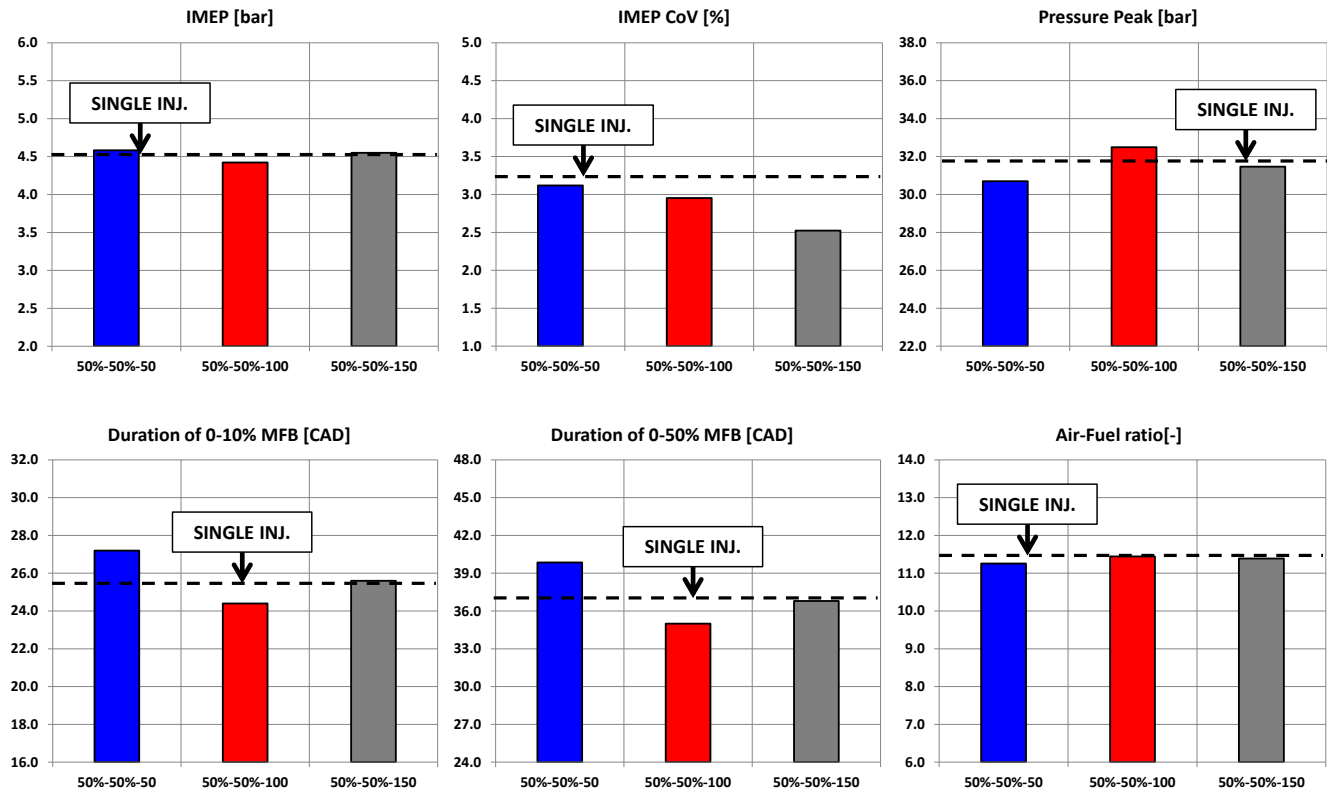


Figure 11: Overall engine output performance for different timings of the second injection pulse.

A relevant effect of the injection strategy is measured on pollutant formation, as summarized in Figure 12. For a longer relative duration of the second pulse (i.e. for a greater injected mass), smoke opacity and particulate emissions increase. The same happens when delaying the start of the second injection. This effect is related to the low volatility of n-butanol, which reduces the physical time available for evaporation and mixing, and to the related poor mixture preparation (i.e. low homogeneity). A non-negligible smoke opacity reduction is measured for most of the split injection strategies compared to the single one, if extremely delayed injections are avoided (e.g. the 30%-70%-100 or the 50%-50%-150 cases).

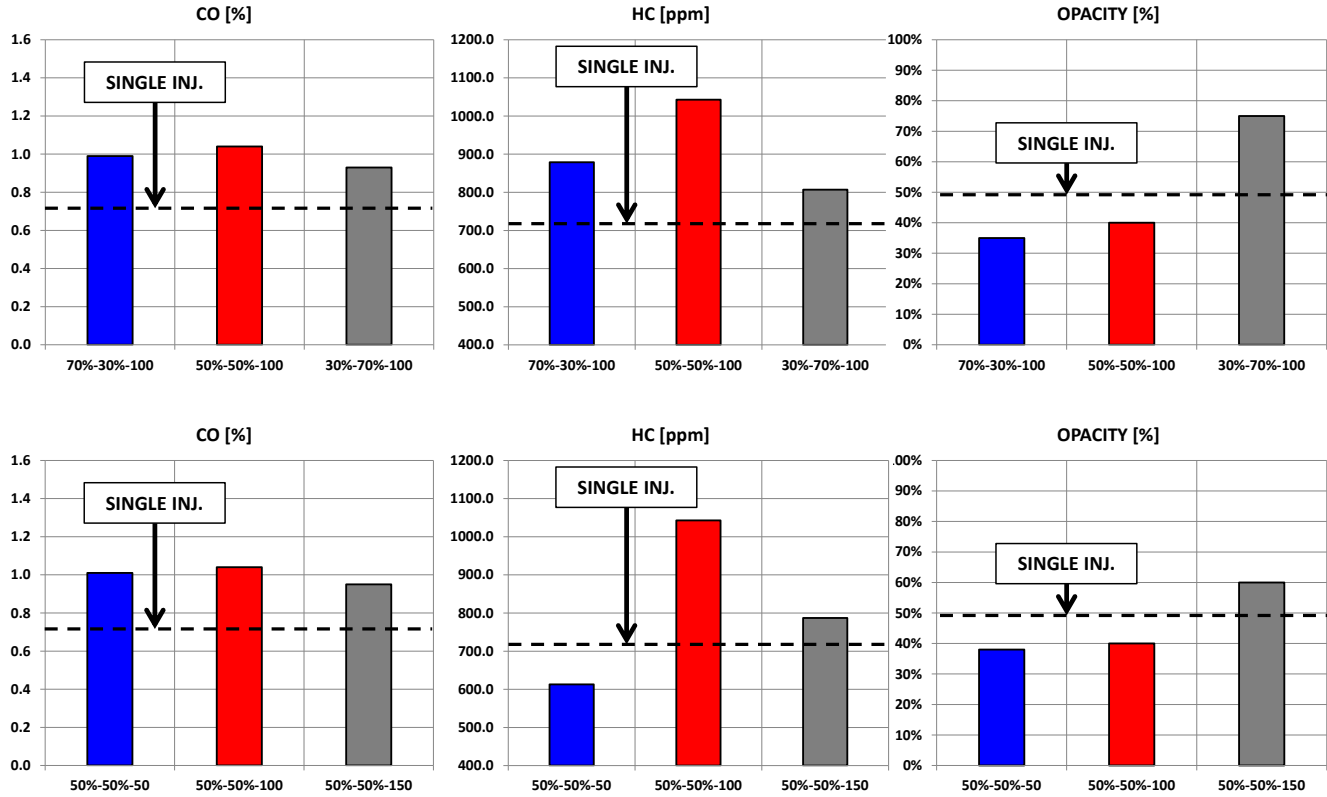


Figure 12: Measured Emissions (CO, HC and Opacity) when changing injection strategy.

Despite the improved combustion phasing and duration, in most of the split-injection cases an increase in CO and HC emissions is measured, compared to the single injection one. Such general increase using split injection strategies seems to be more related to the optical engine peculiar layout (e.g. the large piston skirt-liner crevice volume and the relevant blow-by flow rate) than to mixture preparation itself. With the single injection strategy and SOI 300 CAD bTDC, the injection terminates within the first half of the intake stroke while, using split injection, the end of injection moves at the final stages of the intake or during the compression stroke: this means that a high liquid phase fraction is still present during the ignition phase. Close to the TDC both the piston motion and the increase in the blow-by mass flow rate promote crevices filling. The larger fuel quantity trapped in the crevice volume cannot be consumed during regular combustion, thus promoting CO and HC formation.

3.2 CFD Results

3.2.1 CFD Model Validation: Combustion

The robustness of the developed CFD methodology is assessed by comparing numerical results to experimental measurements using different injection strategies in terms of in-cylinder pressure traces. The average measured in-cylinder pressures and the CFD simulated ones are compared changing the relative injection duration and the timing of the second injection pulse in Figure 13; a comparison between experiments and CFD of early and main combustion durations and global Air Fuel ratio is reported in Figure 14.

The relative trend for variations of the injection strategy is well captured by the CFD model in terms of combustion phasing: similarly to the experiments, a slight decrease of combustion duration with the 50%-50% strategy is shown and a more evident reduction of burn duration with the 70%-30% one is observed. Furthermore, a delayed combustion is simulated for the 30%-70% case, while a minor impact on combustion development is predicted for variations of the phasing of the second injection pulse, in line with the experimental data.

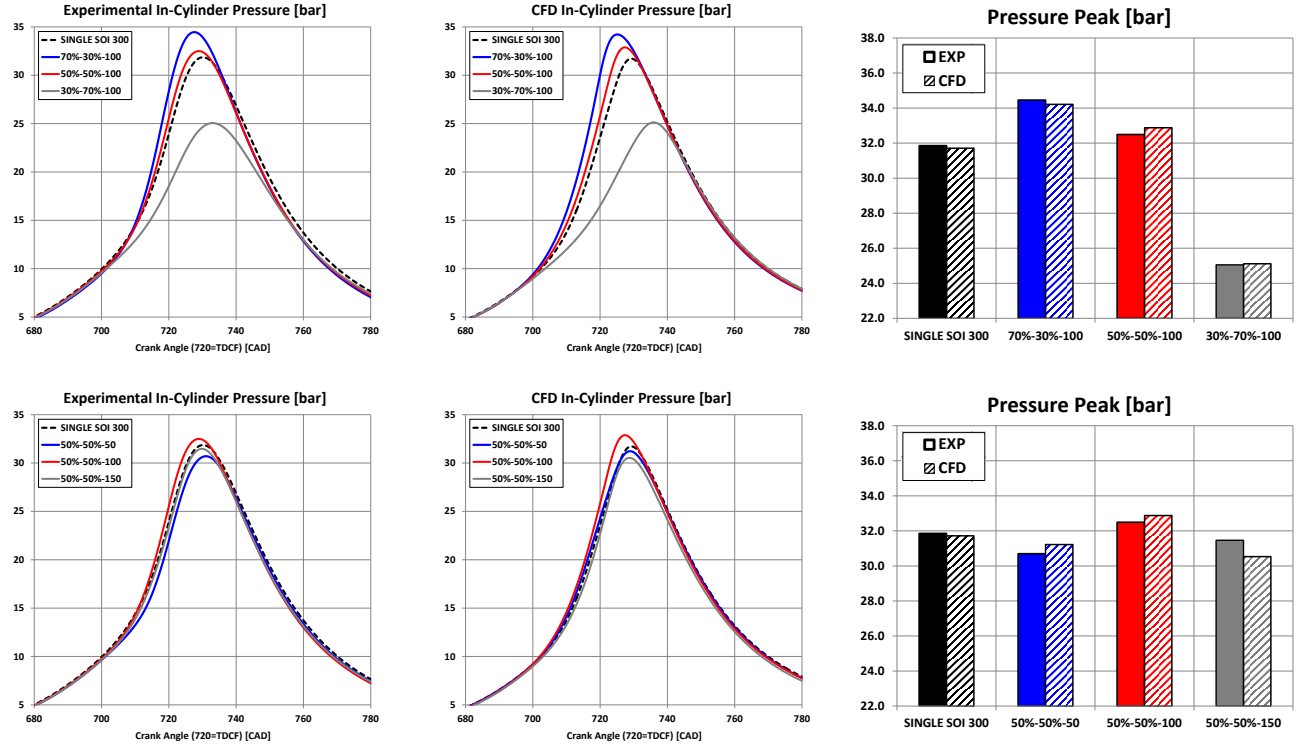


Figure 13: Comparison between experimental and CFD outcomes in terms of in-cylinder pressure traces and pressure peaks for different injection strategies.

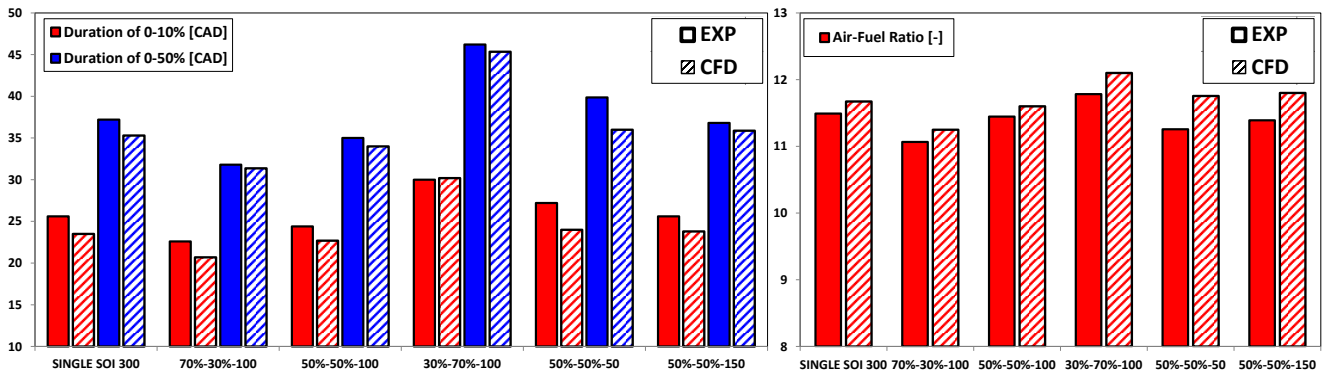


Figure 14: Comparison between experimental and CFD outcomes in terms of early/main combustion duration and air-fuel ratio.

Combustion durations are generally slightly underestimated by CFD (the relative error is lower than 10%) but the relative trend between the cases is reasonably well reproduced without any case specific model tuning. Conversely, air to fuel ratio is slightly overestimated in all cases due to an overestimation of trapped air mass on equal injected fuel.

On equal fuel delivery and spark timing between all the analyzed cases the primary role of charge stratification on combustion onset and flame development using n-butanol is clearly visible from both experiments and CFD simulations. The model is reasonably reliable in predicting relatively differences in combustion behavior when changing the injection strategy, and it will be used to understand at a fundamental level the reasons behind the measured trends. At first, the interaction between the spray plumes and the in-cylinder flow field, in turn leading to different wall impingement and charge stratification, is analyzed for the different injection strategies. Secondly, the impact of different fuel distributions at spark timing on combustion onset and duration, as well as on diffusive flame frequency and intensity, is examined.

3.2.2 Spray-Flow Field Interaction

In a GDI wall-guided architecture the spray plumes orientation and interaction with the in-cylinder flow field strongly affect spray-wall interaction and mixture homogenization. In the current application the substitution of the bowl-shaped piston with a flat one and the adoption of a low evaporating fuel such as n-butanol are critical aspects which must be considered in identifying more effective injection strategies. On one hand an advance in the injection phasing would promote charge homogenization by increasing the mixing time; on the other hand too early an injection would promote fuel deposit formation on the piston crown due to the short distance between the injector tip and the piston itself.

In the specific case, during the first injection pulse, liquid film formation on the piston is particularly promoted by the spray plume orientation (see Figure 1) and the interaction with the in-cylinder flow field. As visible in Figure 15, at the start of the first injection pulse (same SOI_1 for all the analysed cases) an intense flow field pointing towards the piston, forced by the intake curtain flux, is present below the injector tip; such flow field enhances the penetration of the plumes 1, 2 and 3 towards the piston and it deviates plume number 4 towards the same direction.

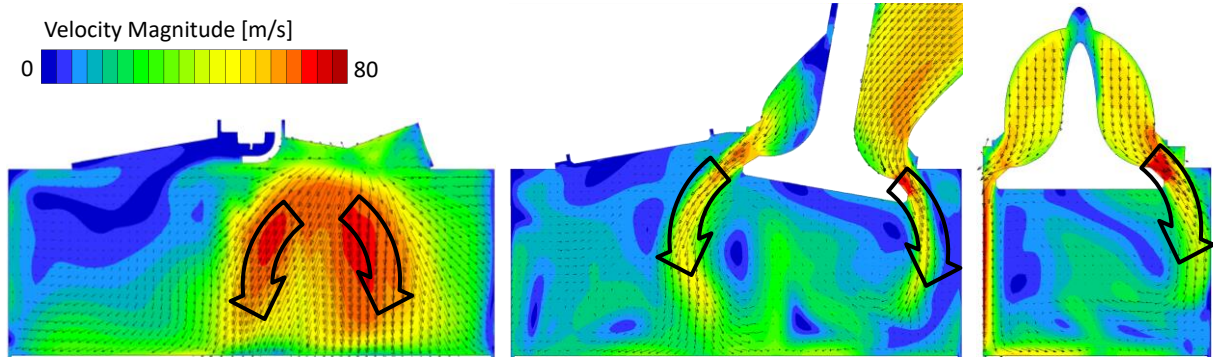


Figure 15: Velocity vectors and magnitude at SOI_1 (300 CAD bTDC) on symmetry plane (left), horizontal intake valve cutting plane (middle) and vertical intake valve cutting plane (right)

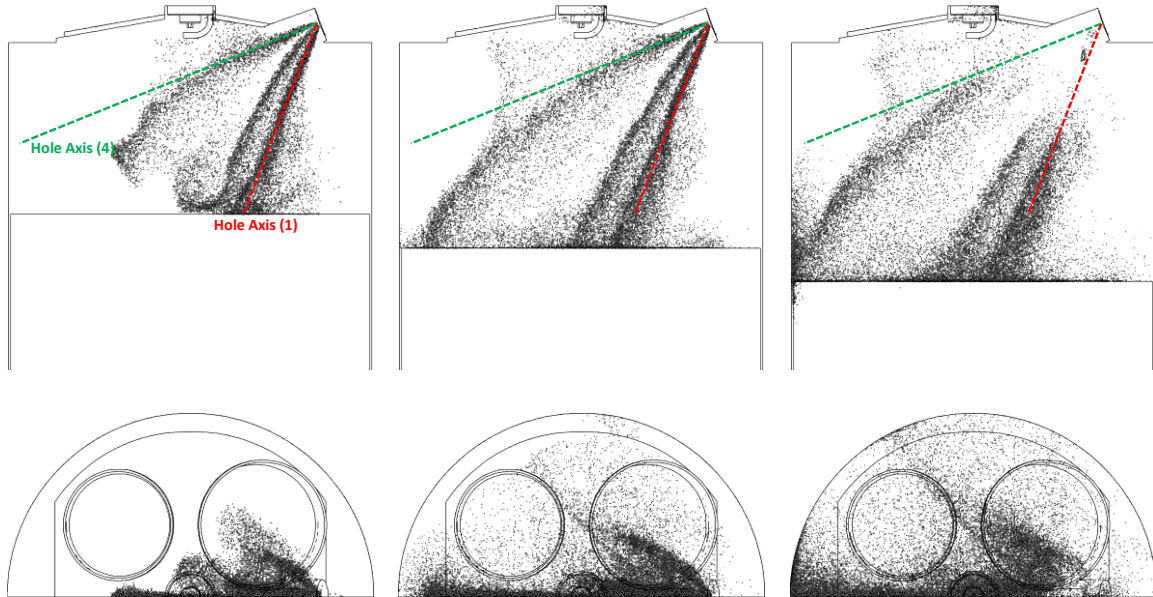


Figure 16: Liquid droplet during the first injection pulse for the 70%-30%-100 injection strategy at 10, 20 and 30 CAD aSOI_1

In Figure 16 spray images during the whole first injection pulse of the 70%-30%-100 injection strategy are reported superimposed to the axes of hole 1 and 4. From the images, the deviation of spray plume number 4 towards the piston due to the tumbling flow field is quite evident; this decreases the penetration of the spray towards the liner and consequently the cylinder wall-wetting. Due to the deviation of plume number 4, the only one targeting the liner, cylinder wall wetting

appears later in the engine cycle and near the piston crown (as highlighted by the red circles in Figure 17); this effect is even more pronounced when increasing the duration of the first pulse, but it is still significantly less important compared to the one on the piston crown. Considering the droplet distribution at 30 CAD aSOI₁ reported in Figure 17 an even richer mixture in the exhaust side of the combustion chamber is expected if the duration of the first injection pulse is increased.

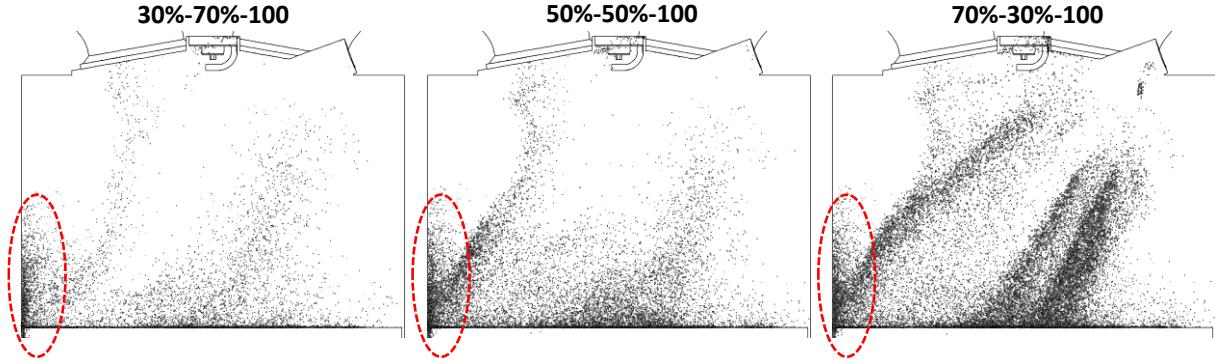


Figure 17: Liquid droplets 30 CAD aSOI₁ for the three different split injection strategies.

Moving from the first to the second injection pulse, i.e. from the first to the second half of the intake stroke (when the delta timing between the 2 injection pulses is 100 CAD) the flow field intensity is reduced with a velocity peak that is halved when moving from 300 to 200 CAD bTDC. As a consequence, the spray-flow interaction is expected to be weaker. Besides the general reduction of flow intensity, the flow direction also changes when switching from SOI₁ to SOI₂, as evidenced in Figure 18; in particular the main flow structure pointing towards the piston, due to the intake curtain flux, is deviated towards the exhaust side, thus enhancing the possibility of fuel deposit formation on the cylinder walls.

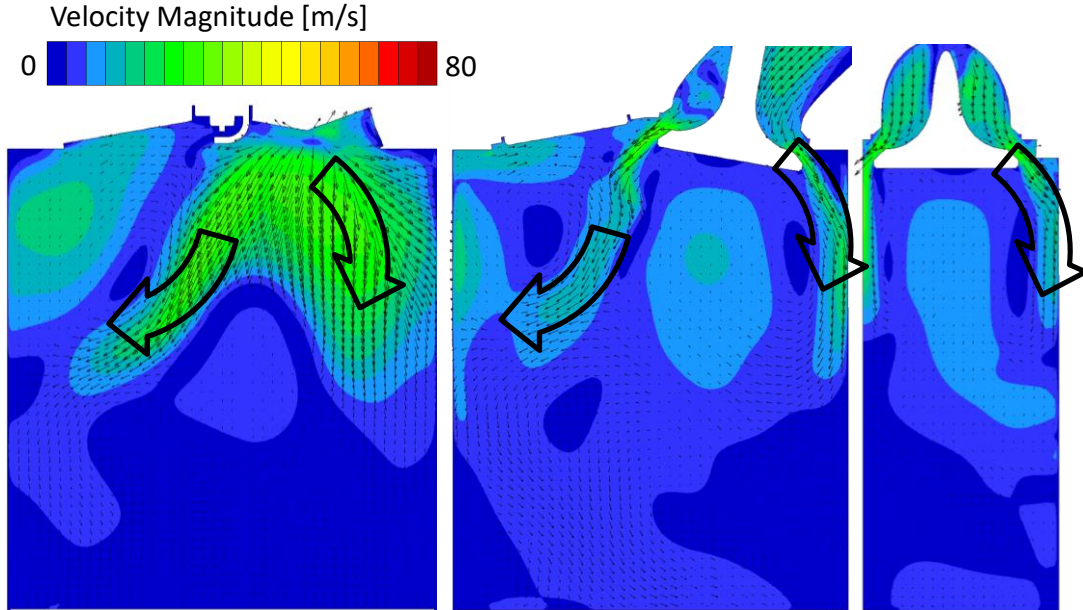


Figure 18: Velocity vectors and magnitude at SOI₂ (200 CAD bTDC) on the symmetry plane (left), horizontal intake valve cutting plane (middle) and vertical intake valve cutting plane (right).

Due to the spray-flow interaction and the short distance between the injector tip and the piston, most of the liquid film is formed on the piston crown during the first injection pulse; conversely liner wetting is non-negligible only with a long/predominant first pulse. The higher distance between the piston crown and the injector tip, together with the different flow structure leads to a more pronounced liner wetting during the second injection pulse which increasing when prolonging the duration of the pulse itself. As visible from the spray images in Figure 19 and highlighted in blue, at 30 CAD aSOI₁

spray plume number 4 reaches the cylinder wall and, 10 CAD later, plumes number 1 and 2 reach the exhaust periphery of the piston crown. This happens in the 30%-70%-100 case, while with a shorter second pulse (70%-30%-100 case) spray wall interaction is generally lower.

In Figure 19, showing the second pulse fuel spray for the two extreme injection strategies in terms of splitting ratio (same SOI_1 and SOI_2), the spray-wall impacting regions of the first and second injection pulses are highlighted in red and blue respectively. With a longer first pulse, higher amount of liquid droplets is found widespread near the piston crown due to the interaction of all the spray plumes with the piston crown (see Figure 16) while with a shorter first pulse the interaction between piston walls and spray is more located on the intake side (red boxes in Figure 19) especially due to plumes 1 and 2.

Generally speaking, the first injection pulse promotes piston wall wetting in all the injection strategies. With a longer first pulse both the intake and the exhaust side of the piston crown are wetted while with a shorter one liquid film is formed in the intake side of the piston only. The second injection pulse promotes increasing liner wetting as pulse duration is higher, for all the injection strategies. With a sufficiently longer second pulse, the exhaust side of the piston crown is wetted as well. Changing the phasing of the second injection pulse has a minor effect on the amount of liner wall wetting, since it changes only in phasing; conversely, either increasing or delaying the distance between the two pulses directly influences piston wall wetting due to the reduced distance between the piston crown and the injector tip.

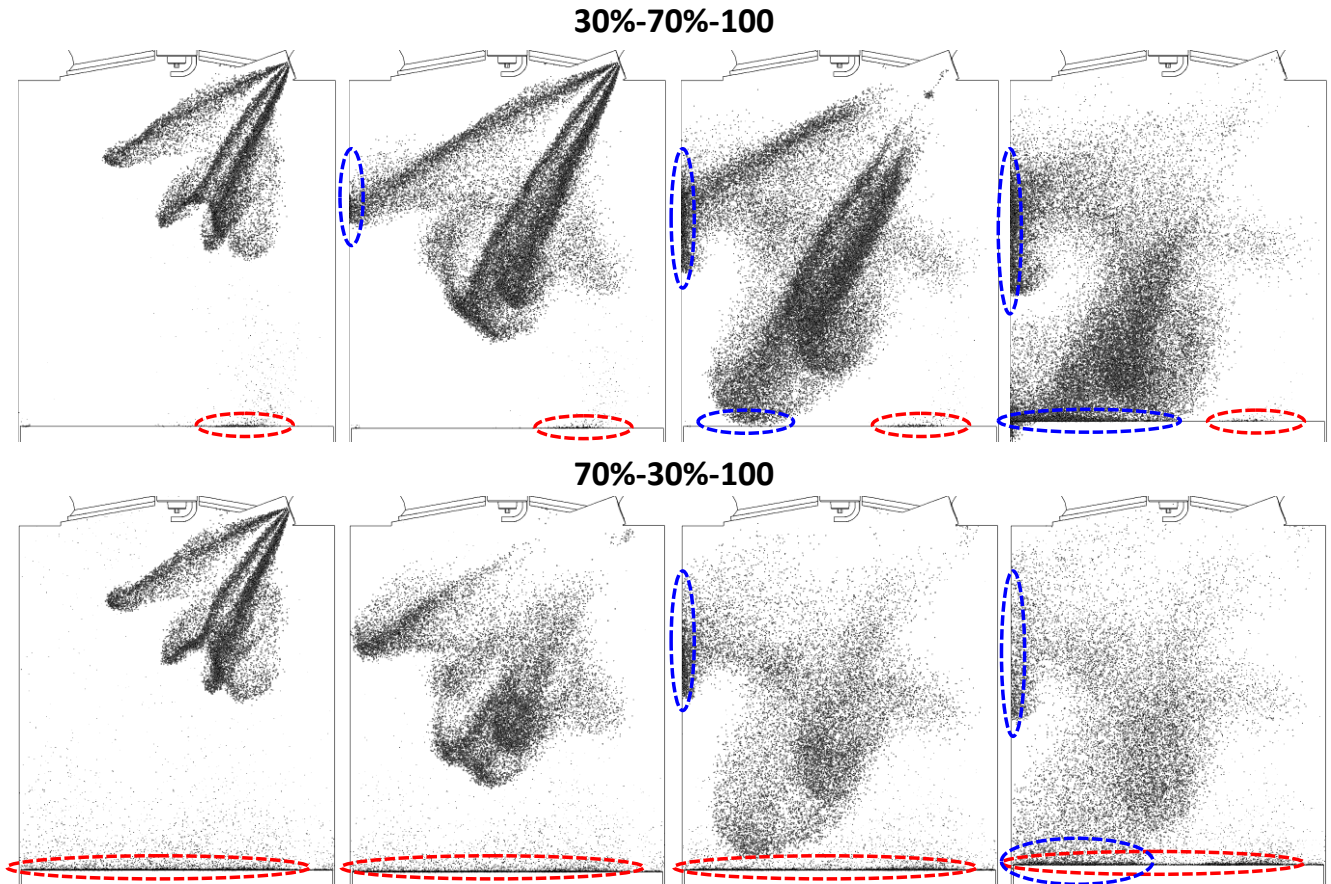


Figure 19: Liquid droplets 10,20,30,40 CAD aSOI_2 for the 30%-70%-100 (top) and the 70%-30%-100 (bottom) injection strategies.

3.2.2 Charge Stratification-Combustion Interaction

The analysis of the CFD results in terms of ER field at spark timing (Figure 20) shows a fuel-enriched zone near the piston crown in all the cases, while the mixture quality is leaner in the spark plug region. This kind of charge stratification is

strongly related to spray-wall interaction and fuel deposit formation on the piston crown, which can involve a significant fraction of the total injected fuel, as high as the 16% (Figure 21). This aspect is more critical compared to gasoline fueling, due to the low evaporating nature of alcohols increasing spray momentum and liquid penetration. All the n-butanol film is evaporated at spark time, however its slow evaporation during the compression stroke affects mixture stratification and causes the rich pockets near the piston crown.

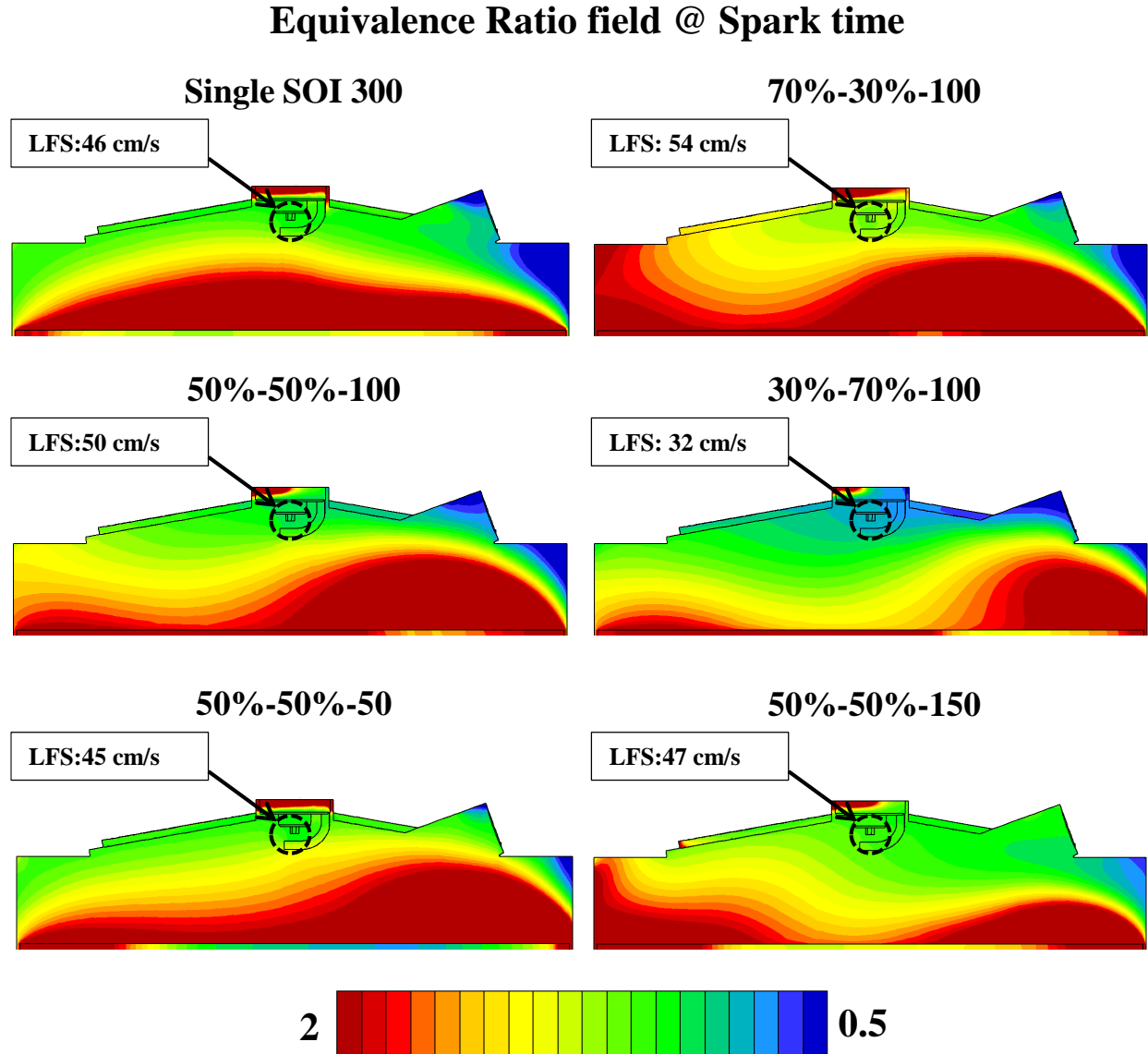


Figure 20: Numerical Equivalence Ratio field at spark timing (30 CAD bTDC).

Despite split injection strategies are unable to fully suppress the presence of rich mixture regions, their adoption is effective in reducing the mass of fuel deposits on the piston crown and in improving charge homogeneity (Figure 21). Shortening the first injection pulse, the first peak of film mass decreases, while another peak (related to the second injection pulses) appears only in cases characterized by at least 50% of fuel mass delivered during the second pulse. The delay of the second pulse timing promotes film formation due to the short piston-injector distance.

Mixture homogeneity at spark timing is evaluated as $1/ER_{RMS}$ by considering the cell-wise local equivalence ratio; in Figure 21 results are normalized with respect to the single injection case. A more homogeneous mixture is obtained with both 50%-50% and 30%-70% strategies compared to the single injection case, while a slight worsening of charge homogeneity is obtained in the 70%-30% case. Despite the delayed longer second injection pulse, charge homogenization is promoted by

the reduction in deposits formation in the 50%-50% and 30%-70% cases; conversely, with a predominant first pulse (70%-30%), the slight reduction in film formation is not sufficient to promote charge homogenization, that is slightly reduced by the delayed EOI (End Of Injection), with respect to the single injection case. The same is observed excessively delaying the second injection pulse due to strongly reduced mixing time. Similarly to the injection timing analysis these two competing aspects (fuel deposits formation and available mixing time) play a fundamental role in the design of the split-injection strategy.

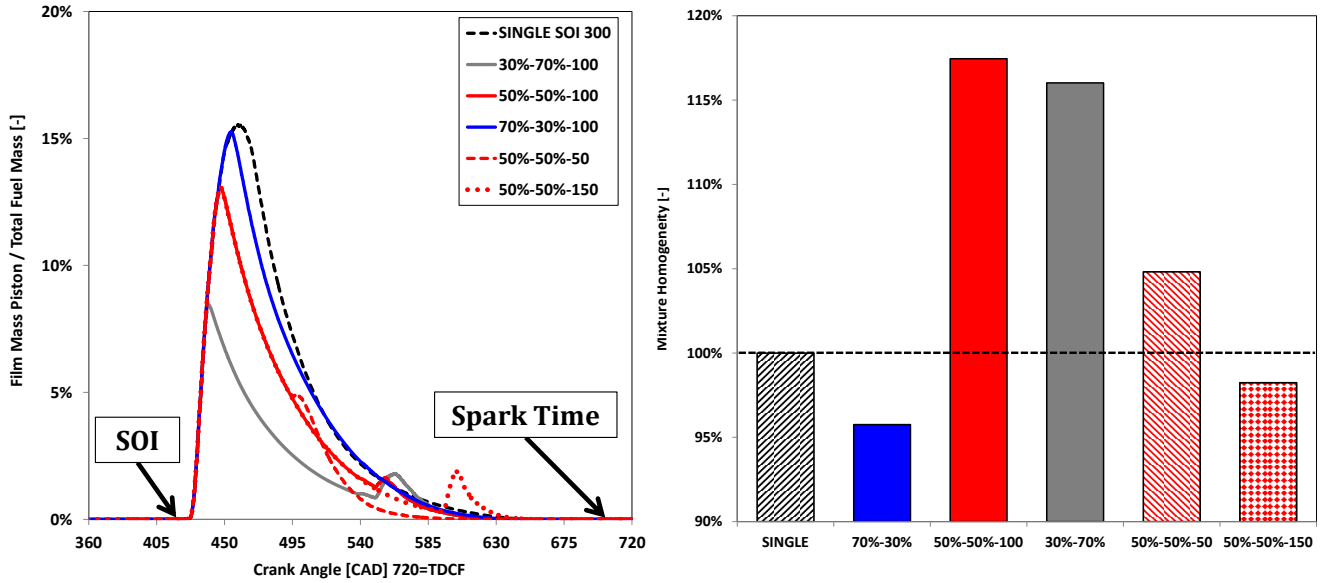


Figure 21: Liquid film mass on the piston crown during the intake and power strokes (left) and charge homogeneity ($1/ER_{RMS}$) at spark timing (right) for all the tested injection strategies.

Spray and Liquid film (30%-70%-100 Case)

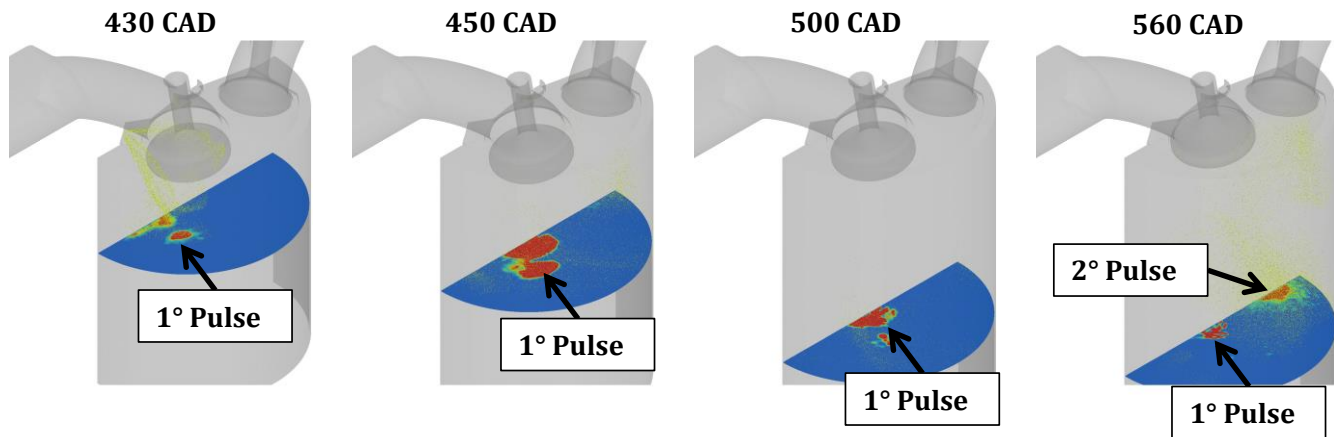


Figure 22: Droplets (yellow) and liquid deposit thickness during intake and compression strokes for the 30%-70%-100 case.

The different spray-wall interaction affects also the ER distribution at spark timing (Figure 20): the shape of the rich pocket near the piston crown moves from a quasi-symmetric shape (with respect to the cylinder axis) when using the single injection strategy, to a less symmetric one for the split cases; for these latter, the rich pocket moves from the center of the

combustion chamber towards the intake side. The extension of the rich zone is linked to the relative pulse duration, and it is strongly reduced by an increase of the second injection pulse duration as a consequence of a deposit reduction. Delaying the second pulse, the shape of the rich zone becomes even more binomial changing from a single pocket centered in the intake side for the 50%-50%-50 case to two separate regions (one in the intake side, one in the exhaust one) for the 50%-50%-150 case. This effect is strongly related to the impact zone of the spray on the piston. In Figure 22 a contour of the liquid film thickness superimposed to the liquid spray droplets is reported for the 30%-70% case. The interaction between spray plumes, flow field and piston motion leads to the formation of deposits in the intake side after the first injection pulse. Delaying the second pulse, this effect is increased by the piston motion, determining more prominent formation of deposits near the exhaust side; this in turn leads to rich mixture pockets close to the piston crown in that region, particularly for the 30%-70%-100, 50%-50%-100 and 150 cases.

Charge stratification variation due to changes in spray-wall interaction for different injection strategies has a relevant impact on mixture quality and consequently on the LFS in the spark plug region. The presence of wide rich pockets in the intake side, along with the residual tumble motion (oriented from the intake to the exhaust side in the upper part of the combustion chamber) leads to a mixture “enrichment” in the spark plug region for the 70%-30%-100 and 50%-50%-100 cases, compared to single injection one. This results in a shorter early burn duration and advanced combustion phasing. Conversely, with the reduced intake side enrichment of the 30%-70%-100 case, mixture quality in the spark plug region is leaner and the burn duration strongly increases.

The LFS_{spark} reduction due to charge leaning is the root cause behind the very slow burn rate and delayed combustion measured in the 30%-70% case. The strong relationship found in all the cases between combustion durations, spark mixture quality and LFS_{spark} is highlighted in Figure 23. With respect to the single injection case (local ER=0.97 near the spark plug), local charge enrichment leads to a higher LFS_{spark} and to a reduced combustion duration; the opposite is verified for the 30%-70%-100 case, due to further charge leaning, causing a consistent drop in the LFS_{spark} and a strong increase of burn duration. The same considerations are valid for all the analyzed cases, as confirmed by the reverse trend between local LFS_{spark} at ignition and combustion durations.

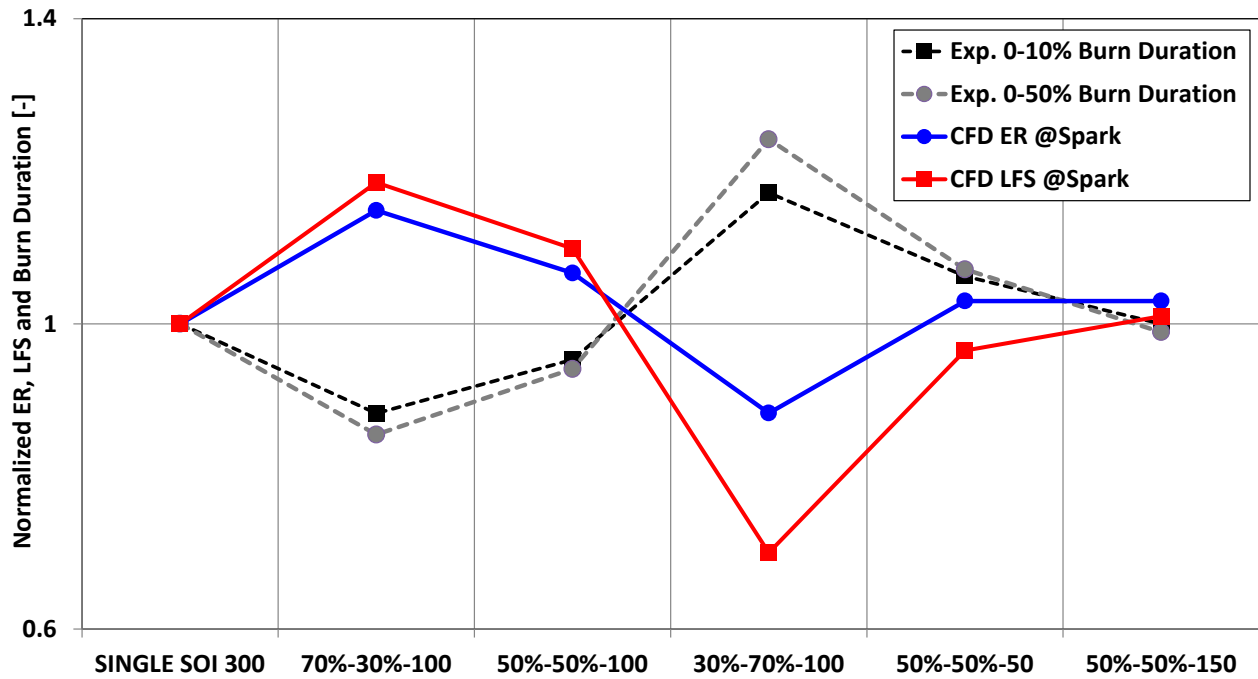
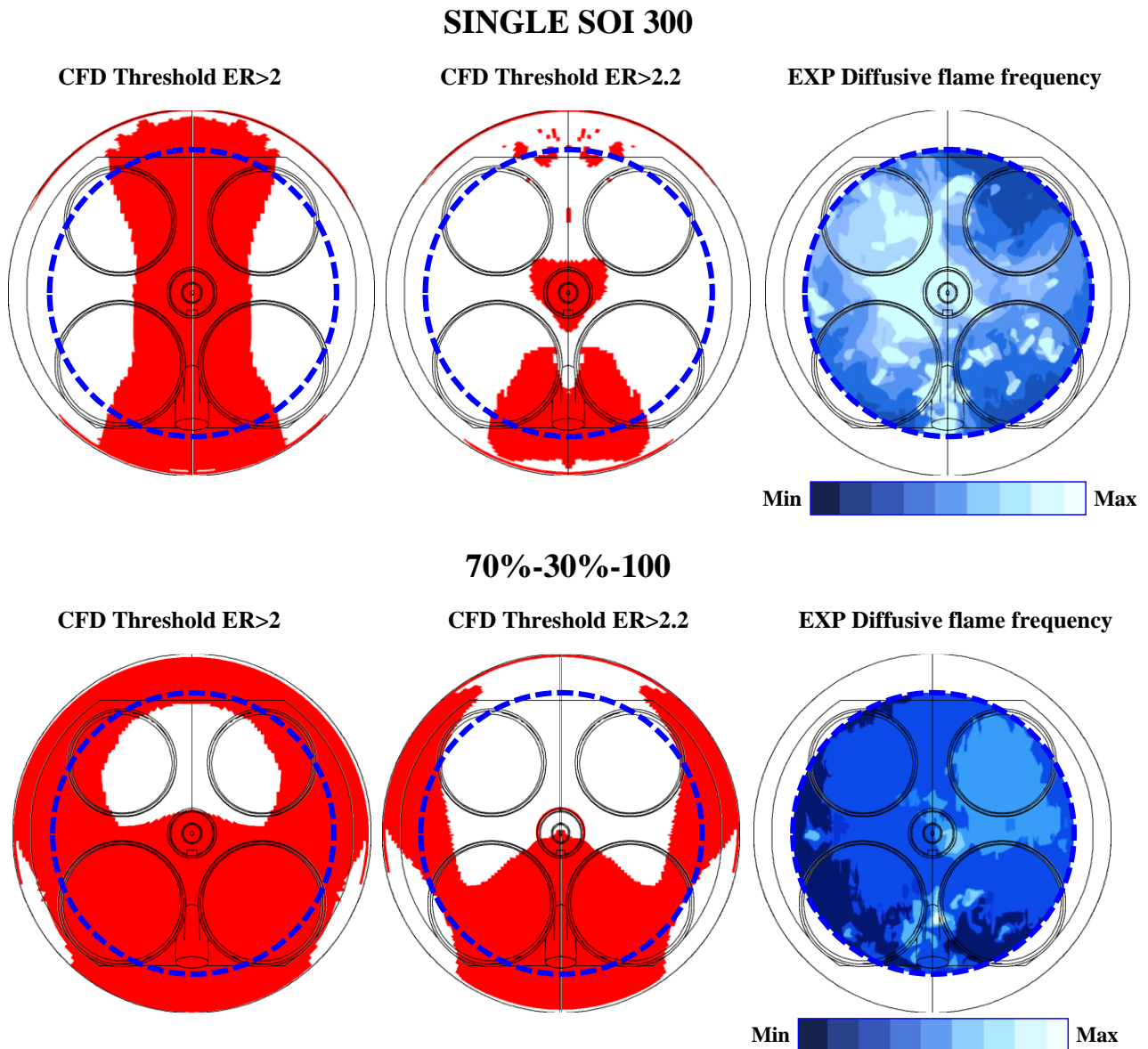


Figure 23: Normalized CFD equivalence ratio and laminar flame speed in the spark region at spark time and normalized experimental early and main burn duration.

3.3 Optical analysis and comparison with CFD

Optically measured diffusive flame frequency maps are compared in Figure 24 to simulated thresholds of ER higher than 2 and 2.2. A strong correlation between diffusive flames probability and predicted rich regions within the combustion chamber at spark timing is observable in all the cases, further confirming the key role of mixture quality on combustion mode and soot formation, as outlined by the purely chemical kinetic study (Figure 9).

Except for the single injection case, the maximum probability of diffusive flames was always measured in the intake side of the combustion chamber (near the injector), where the CFD model predicts a rich mixture pocket for all the injection strategies, related to fuel deposits formation on the piston crown after the first injection pulse. Generally a more symmetric probability is measured in the single injection case, as confirmed by the more symmetric shape of the ER>2 region comparing the intake and exhaust sides.



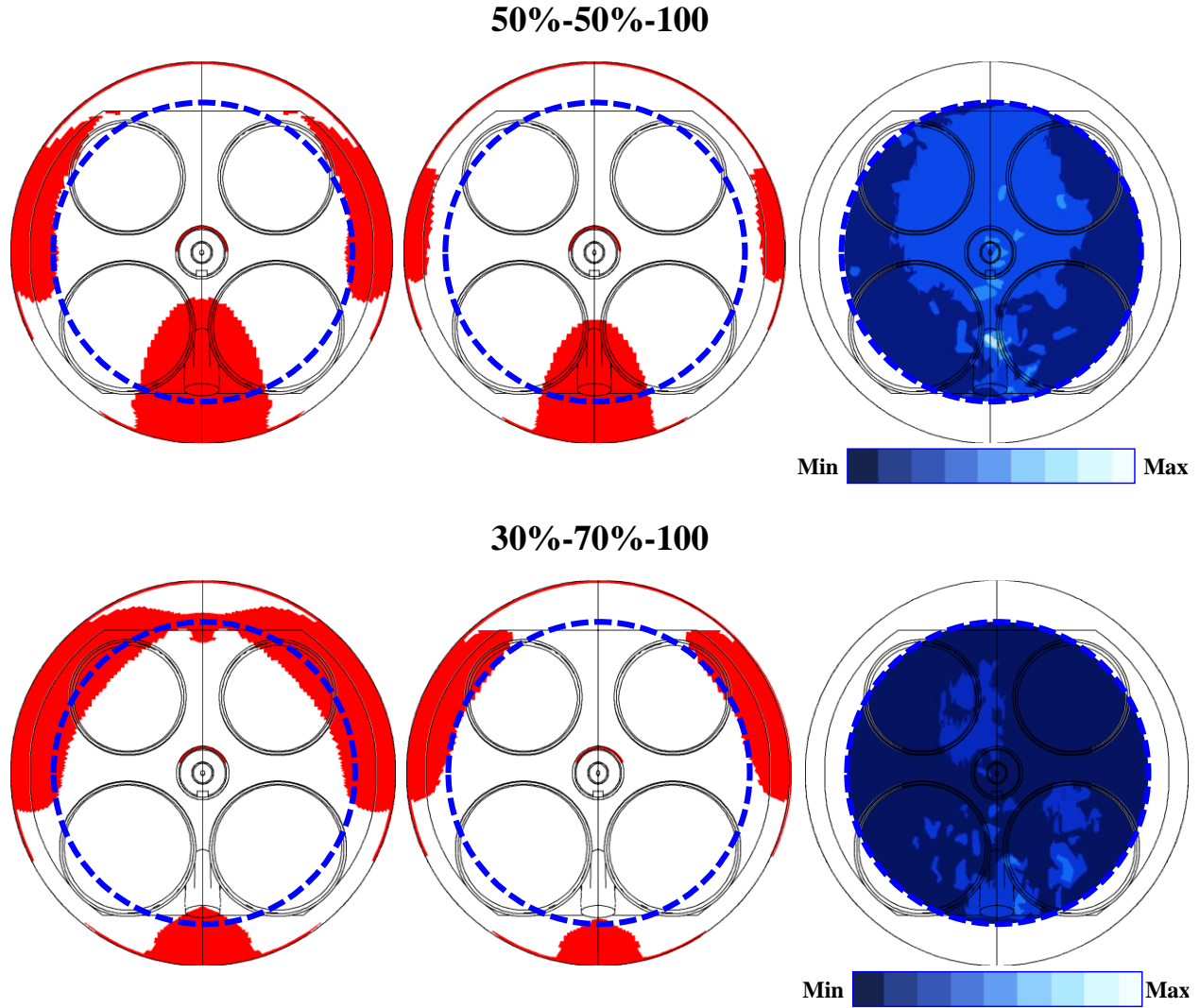


Figure 24: Region with $ER > 2$ (left) and $ER > 2.2$ (middle) from numerical simulations at spark timing (30 CAD bTDC) and experimental diffusive flame probability maps (right), for different relative duration of the two injection pulses.

The intensity of diffusive flames decreases for shortening of the first injection pulse, as well as the extension of the rich region in the optically accessible portion of the combustion chamber in CFD. However, in the 30%-70%-100 case, a non-null probability to have diffusive flame is measured on the intake side, also suggested by the analysis of fuel film distribution predicted by the CFD model (Figure 22).

A further confirmation of the robustness of the CFD model in the prediction of mixture preparation can be found by analyzing changes in the location of diffusive flame frequency, when varying the phasing of the second injection pulse for the 50%-50% strategy (Figure 25). The probability to find diffusive flames in the exhaust side of the combustion chamber increases when delaying the second injection pulse. The size of the rich pocket predicted by the CFD model in the same region increases coherently, with a simultaneous reduction of the rich region near the intake.

From a quantitative point of view, a direct comparison is carried out between the diffusive flame area (based on optical measurements) and the extension of the rich zones ($ER > 2$ at 30 CAD bTDC in CFD simulations). These results are reported in the histogram of Figure 26, normalized with respect to the single injection case. Two different CFD results are reported, in the first one (red bars) the area beyond the optical limit is not included in the analysis (as in the experiments) while in the second one (blue bars) the full bore geometry is considered.

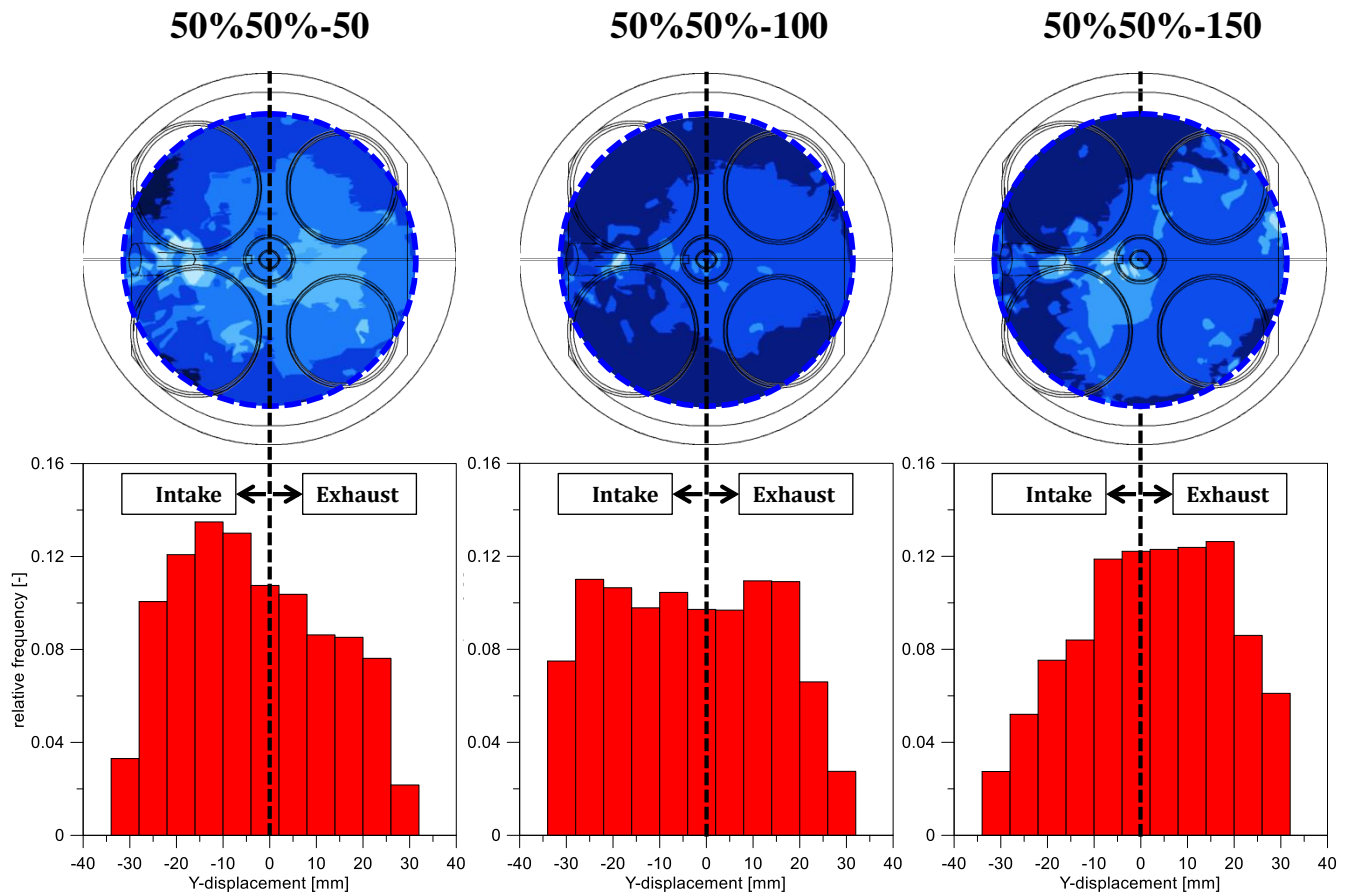


Figure 25: Experimental diffusive flame probability maps when changing the phasing of the second injection pulse for the 50%-50% split injection strategy (top) and PDF of diffusive flame locations (bottom).

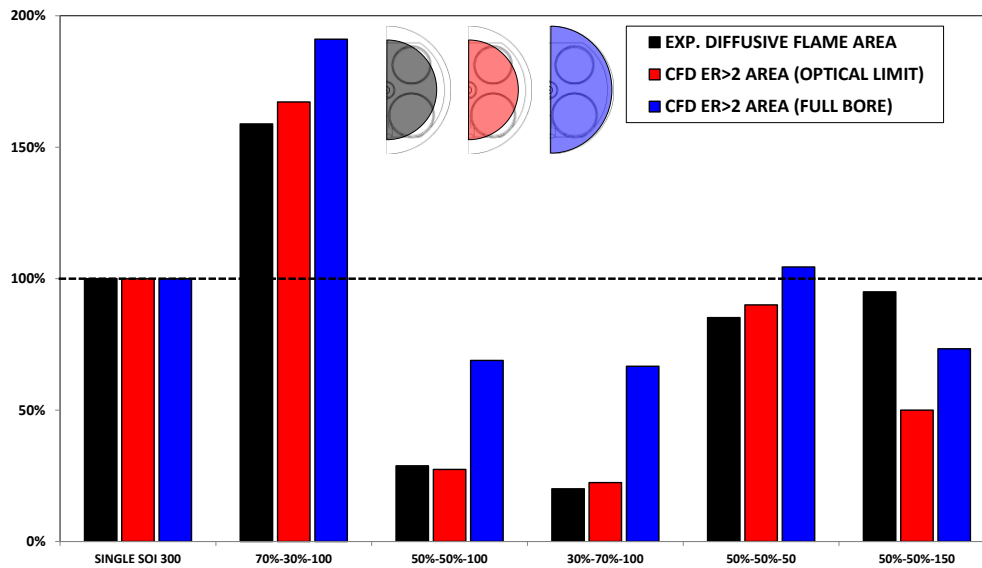


Figure 26: Comparison between CFD areas with ER greater than 2 and experimental diffusive flame areas (normalized with respect to the single injection case).

A satisfying agreement is found when comparing experimental and CFD data, by using the same geometrical threshold represented by the optically accessible area; differences between the injection strategies are underestimated considering the full-bore geometry when post-processing the CFD data. This is emphasized for the 50%-50%-100 and 30%-70%-100 cases, for which most of the rich mixture zones are in the optically inaccessible portion of the combustion chamber, near the cylinder wall. The overall trend does not significantly change, considering the optical equivalent area or the full piston surface in the CFD results.

From this standpoint, the “worst” injection strategies are those injecting a higher amount of fuel early during the cycle (i.e. the 70%-30% and 50%-50%-50), showing a greater tendency to promote diffusive combustion compared to the single injection case. Conversely, a reduced tendency towards sooting diffusive flames is found with the 50%-50%-100 and 30%-70%-100 strategies, even if the advantage can be potentially reduced considering the whole combustion chamber. These results demonstrate that the potential benefit of early injection of low evaporating fuels might be reduced by charge preparation issues, due to the increase in fuel deposits formation leading to relevant charge stratification.

3.4 Soot Emission Analysis

Diffusive flames are responsible for soot precursor species production. In particular, according to the purely chemical kinetic study in Figure 9, air-butanol mixtures with an $ER > 2$ and temperature in the range of 600-1200K are responsible for maximum soot precursor species formation. The strong correlation between rich mixture pockets and diffusive flames is confirmed by the CFD results; however, optical measurements and CFD results are apparently not correlated with the measured smoke opacity. In particular, changing the relative duration of the two injection pulses (70%-30%-100 and 30%-70%-100), an opposite trend with respect to the experimental data is found.

A first explanation for the lack of correlation is found in the optical limit considering that the near-wall portion of the combustion chamber is optically blind. A partial confirmation of this can be found by monitoring rich mixture pockets in CFD results beyond the optical limit, as reported in Figure 26, and quantifying the impact of the whole cylinder bore instead of the optically accessible portion. This kind of analysis is carried out by defining the amplification index I_A (Equation 4) and comparing the fraction of the optical and full bore area covered by rich mixtures ($ER > 2$). The value of the I_A index for all the analyzed injection strategies is reported in the histogram of Figure 27.

$$I_A = \left(\frac{\text{Area } ER > 2 \text{ Optical}}{\text{Area Optical}} \right) \bigg/ \left(\frac{\text{Area } ER > 2 \text{ Full Bore}}{\text{Area Full Bore}} \right) \quad (\text{Equation 4})$$

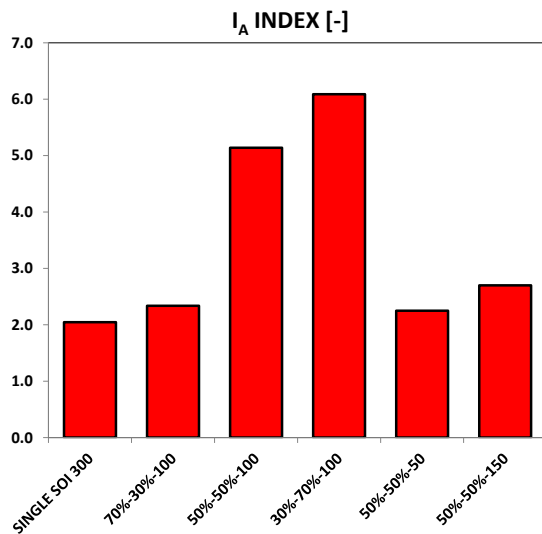


Figure 27: Amplification index I_A for the tested injected strategies.

Considering as reference area the entire piston area instead of the optically accessible portion, the fractional presence of rich mixture pockets ($ER > 2$) increases ($I_A > 1$), suggesting that the near-wall region is generally richer than the core for all the analyzed injection strategies. However, the optically accessible area is sufficiently representative of the whole combustion chamber in most cases ($2.0 < I_A < 3.0$), except for the 50%-50%-100 and the 30%-70%-100 ones, for which I_A is consistently higher. This suggests that in these two cases most of the soot-promoting rich mixture lies outside the optically accessible area, leading to uncorrelated frequency of diffusive flames and smoke opacity. As confirmed by the data in Figure 27, the soot formation tendency is underestimated in the cases in which the I_A index is greater than 3.0 (i.e. 50%-50%-100 and 30%-70%-100). Nevertheless, even accounting for rich mixtures beyond the optical limit (blue bars in Figure 26) the relative trend between 30%-70% and 70%-30% is unaffected: this means that the optical limit alone does not fully justify the inconsistency between experimental measurements and CFD results.

However, measured engine-out particulate emission is the consequence of two competing mechanisms: soot production and oxidation, i.e. low smoke opacity can be caused by low particle production, in turn favored by high charge homogeneity, but also by effective soot oxidation. As reported in Figure 9, soot oxidation rate is promoted when mixture temperature is over 1800 K, while it is negligible for temperatures below 1200 K. Average temperature evolution as a function of the equivalence ratio in the combustion chamber from CFD simulation is superimposed to the oxidation rate map in Figure 28, with the aim of underlining differences between the analyzed injection strategies in terms of soot formation and oxidation tendency.

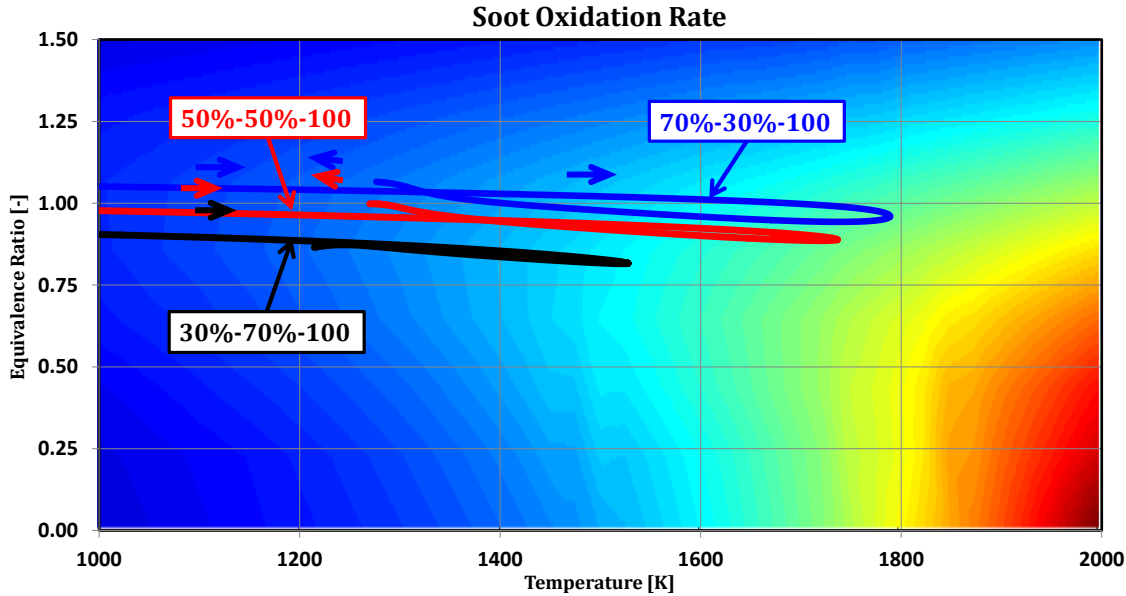


Figure 28: Average in-cylinder temperature and equivalence ratio superimposed to the soot oxidation rate map.

Due to lean mixture formation in the spark region when using the 30%-70%-100 injection strategy, a very delayed combustion phasing was found in both the experiments and the CFD simulations. The delayed combustion phasing for a fixed spark timing leads to a consistent reduction of the average temperature level in the combustion chamber, thus generally resulting in a poor soot oxidation process (Figure 28). Adopting both 70%-30%-100 and 50%-50%-100 injection strategies, the in-cylinder mixture reaches thermal levels able to promote soot oxidation.

Considering as representatives of soot production both optical diffusive flame areas and CFD rich mixture extension (Figure 26), the 50%-50%-100 and 30%-70%-100 injection strategies show very similar soot formation tendency while a higher smoke opacity is measured in the 30%-70%-100 case: this is ascribed to the effectiveness of soot oxidation. Similarly, the low smoke opacity measured for the 70%-30% injection strategy has to be attributed to high soot oxidation rates despite the ineffective charge preparation and the high measured diffusive flame frequency. Another factor which must be considered is related to the delayed EOI of the 30%-70% case, in which 0.8% (about 0.2 mg) of the injected fuel is still liquid at combustion onset: this is not verified using the other injection strategies and it is considered as an additional factor contributing to the higher smoke opacity measured for this injection strategy.

4. Conclusions

An experimental and numerical study on the potential of split injection strategies to improve mixture preparation in a DISI optical engine fueled with n-butanol is carried out. The aim of the activity is to identify dominant factors for the optimization of the injection strategy when using non-conventional fuels such as low evaporating alcohols. In order to compare split injection strategies to a more conventional single injection one, two sensitivity analyses are carried out:

- Variation of the relative duration of the two injection pulses, for a fixed SOI;
- Variation of the phasing of the second injection pulse, for a fixed relative duration of the two.

The experimental campaign clearly show that variations in the relative duration of the n-butanol injection pulses relevantly impact on combustion velocity/phasing and emissions formation. In particular, the most significant findings are:

- Early and main combustion duration increase for increased duration of the second injection pulse;
- The phasing of the second pulse impacts less on combustion phasing and duration;
- Smoke opacity strongly increases for longer second injection pulse.

Compared to the single injection case:

- An improvement in combustion duration is found injecting at least half of the total mass;
- A reduction of smoke opacity is measured injecting at least half of the total mass in the first pulse.

The same injection strategies are analyzed through a detailed 3D CFD model of the optical engine with the aim to investigate the root causes behind the measured behavior which, with a stand-alone experimental campaign, can be challenging to understand. From a deep analysis of both experimental and CFD results the following conclusions can be drawn:

- Charge stratification at spark time is strongly affected by the interaction between liquid fuel spray and solid walls leading to fuel deposit pools; in order to improve mixture homogeneity pools should be limited as much as possible
- Substituting gasoline with a less evaporating fuel such as n-butanol (without change anything the engine hardware) the worsening in mixture preparation can strongly affect the engine performance in terms of combustion duration and emissions formations
- Mixture quality in the spark region is strongly related to both early and main combustion duration. To improve combustion duration a slightly rich mixture ($1.05 < ER < 1.15$) in the spark region, or generally in the center of the combustion chamber, should be ensured.
- Split injection strategies can help in improving mixture homogeneity reducing spray wall interaction thanks to the reduction of the spray penetration reducing the duration of each single pulse (retaining the same fuel delivery). In particular shortening the first pulse (when the piston is closer to the injector tip) the mass of fuel deposits can be strongly reduced.
- A strong correlation is found between rich mixture pockets ($ER > 2$) and diffusive flame onset both in terms of frequency and location.
- In the current application a longer first injection pulse helps in enriching charge stratification at spark improving combustion helping also in reducing fuel film formation with respect to a single injection strategy.
- Retaining a longer first injection pulse and optimizing the phasing of the second one, split injection strategies are found to be a promising solution to improve charge homogeneity, to reduce deposit formation and at the same time to improve mixture quality in the spark plug region. Therefore they are found to be favorable strategies to improve combustion development when using low evaporating alcohols such as n-butanol.

5. References

1. Peters J F, Iribarren D, Dufour J. Simulation and life cycle assessment of biofuel production via fast pyrolysis and hydro upgrading. Fuel 2015; 139:441-56.
2. DIRECTIVE 2009/28/EC OF THE EUROPEAN PARLIAMENT AND OF THE COUNCIL of 23 April 2009. Official Journal of the European Union 2009; 16–63.

3. Garcia R, Pizarro C, Lavín A, Bueno J. Biomass sources for thermal conversion. Techno-economical overview. *Fuel* 2017; 195:182–89.
4. Awad O I, Mamat R, Ali O M, et al. Alcohol and ether as alternative fuels in spark ignition engine: A review. *Renewable and sustainable energy reviews* 2018; 83(3):2586-05.
5. Vassilev S V, Vassileva C G, Vassilev V S. Advantages and disadvantages of composition and properties of biomass in comparison with coal: An overview. *Fuel* 2015; 158:330-50.
6. Ujor V, Bharathidasan A, Cornish K, Ezeji T. Feasibility of producing butanol from industrial starchy food wastes. *Applied Energy* 2014; 136:590-98.
7. Koç M, Sekmen Y, Topgül T, Yücesu H S. The effects of ethanol–unleaded gasoline blends on engine performance and exhaust emissions in a spark-ignition engine. *Renewable Energy* 2009; 34:2101–06
8. Berni F, Breda S, d'Adamo A, Fontanesi S, et al. Numerical Investigation on the Effects of Water/Methanol Injection as Knock Suppressor to Increase the Fuel Efficiency of a Highly Downsized GDI Engine. *SAE Technical Paper* 2015-24-2499
9. Canakci M, Ozsezen A N, Alptekin E, Eyidogan M. Impact of alcohol–gasoline fuel blends on the exhaust emission of an SI engine. *Renewable Energy* 2013; 52:111–117
10. Wei H, Feng D, Pan M, Pan J Y, Rao X, Gao D. Experimental investigation on the knocking combustion characteristics of n-Butanol gasoline blends in a DISI engine. *Applied Energy* 2016; 175:346-355
11. Irimescu A, Tornatore C, Merola S, Valentino G. Combustion Process Investigation in a DISI Engine Fuelled with n-Butanol Through Digital Imaging and Chemiluminescence. *SAE Technical Paper* 2015-01-1887
12. Szwaja S, Naber J. Combustion of n-butanol in a spark-ignition IC engine. *Fuel* 2010; 89:1573-82
13. Yaoyao Y, Dong L. Effects of butanol isomers additions on soot nanostructure and reactivity in normal and inverse ethylene diffusion flames. *Fuel* 2017; 205:109-12
14. Aleiferis P, Serras-Pereira J, Richardson D. Characterisation of flame development with ethanol, butanol, iso-octane, gasoline and methane in a direct-injection spark-ignition engine. *Fuel* 2013;109:256-78
15. Serras-Pereira J, Aleiferis P, Richardson D. Imaging and heat flux measurements of wall impinging sprays of hydrocarbons and alcohols in a direct-injection spark-ignition engine. *Fuel* 2012; 91(1):264-97
16. Irimescu A, Marchitto L, Merola S, Tornatore C, Valentino G. Combustion process investigations in an optically accessible DISI engine fuelled with n-Butanol during part load operation. *Renewable Energy* 2015; 77:363-76
17. Breda S, d'Adamo A, Fontanesi S, D'Orrico F, et al. Numerical Simulation of Gasoline and n-Butanol Combustion in an Optically Accessible Research Engine. *SAE International Journal of Fuels and Lubricants* 2017; 10(1):32-55
18. Breda S, d'Adamo A, Fontanesi S, Del Pecchia M, et al. CFD Optimization of n-Butanol Mixture Preparation and Combustion in an Research GDI Engine. *SAE Technical Paper* 2017-24-0063
19. Irimescu A, Merola S, Di Iorio S, Vaglieco B M. Investigation on the effects of butanol and ethanol fueling on combustion and PM emissions in an optically accessible DISI engine. *Fuel* 2018; 216:121-41
20. Bowditch F. A New Tool for Combustion Research A Quartz Piston Engine. *SAE Technical Paper* 1961 610002
21. Merola S, Irimescu A, Marchitto L, Tornatore C, Valentino G. Effect of injection timing on combustion and soot formation in a direct injection spark ignition engine fueled with butanol. *International Journal of Engine Research* 2016; 18(5-6):490-504
22. Irimescu A, Merola S, Martinez S. Influence of engine speed and injection phasing on lean combustion for different dilution rates in an optically accessible wall guided spark ignition engine. *SAE Technical Paper* 2018-01-1421
23. Irimescu A, Tornatore C, Marchitto L, Merola S. Compression ratio and blow-by rates estimation based on motored pressure trace analysis for an optical spark ignition engine. *Applied Thermal Engineering* 2013; 61(2):101-9
24. Irimescu A, Merola S, Di Iorio S, Vaglieco B M. Biofuel effect on flame propagation and soot formation in a DISI engine. In *IOP Conference Series: Materials Science and Engineering* 2017; 252(1)
25. Oliver M A. Kriging: A Method of Interpolation for Geographical Information Systems. *International Journal of Geographic Information Systems* 1990; 4:313–32
26. Berni F, Cicalese G, Fontanesi S. A modified thermal wall function for the estimation of gas-to-wall heat fluxes in CFD in-cylinder simulations of high performance spark-ignition engines. *Applied Thermal Engineering* 2017; 115:1045-62
27. Berni F, Fontanesi S, Cicalese G, d'Adamo A. Critical Aspects on the Use of Thermal Wall Functions in CFD In-Cylinder Simulations of Spark-Ignition Engines. *SAE International Journal of Commercial Vehicle* 2017; 10(2):547-561
28. Giovannoni N, Breda S, Paltrinieri S, d'Adamo A, et al. CFD Analysis of the Effects of Fuel Composition and Injection Strategy on Mixture Preparation and Fuel Deposit Formation in a GDI Engine. *SAE Technical Paper* 2015-24-2408
29. Cavicchi A, Postrioti L, Giovannoni N, et al. Numerical and experimental analysis of the spray momentum flux measuring on a GDI injector. *Fuel* 2017; 206:614-27
30. Han Z, Parrish S, Farrell P V, Reitz R D. Modeling Atomization Processes of Pressure-Swirl Hollow-Cone Fuel Sprays. *Atomization and Sprays* 1997; 7(6):663-684
31. Kuensberg Sarre C, Kong SC, Reitz RD. Modelling the Effects of Injector Nozzle Geometry on Diesel Spray. *SAE Technical Paper* 1999-01-0912
32. Breda S, d'Adamo A, Fontanesi S, Giovannoni N, et al. CFD Analysis of Combustion and Knock in an Optically Accessible GDI Engine. *SAE International Journal of Engines* 2016; 9(1):641-56
33. d'Adamo A, Breda S, Fontanesi S, et al. A RANS knock model to predict the statistical occurrence of engine knock. *Applied Energy* 2017; 191:251-263
34. Rosa NG, Villedieu P, Dewitte J, Lavergne G. A new droplet-wall interaction model. Tenth international conference on liquid atomization and spray systems 2006; Paper ID ICLASS06-167
35. Habchi C, Foucart H, Baritaud T. Influence of the wall temperature on the mixture preparation in DI gasoline engine. *Oil & Gas Science Technology* 1999; 54(2):211-22

36. Colin O, Benkenida A. The 3-Zones Extended Coherent Flame Model (ECFM3Z) for Computing Premixed/Diffusion Combustion Oil & Gas Science and Technology 2004; 59:593-609.
37. Boudier P, Henriot S, Poinot T, Baritaud T. A Model for Turbulent Flame Ignition and Propagation in Spark Ignition Engines Twenty-Fourth Symposium (International) on Combustion/The Combustion Institute 1992, 503-510.
38. Frassoldati R, Grana T, Faravelli E, Ranzi P, Obwald K, Kohse-Hoinghaus. Detailed kinetic modelling of the combustion of the four butanol isomers in premixed low-pressure flames. Combustion and Flame 2012; 159:2295-311
39. d'Adamo A, Del Pecchia M, Breda S, Berni F, et al. Chemistry-Based Laminar Flame Speed Correlations for a Wide Range of Engine Conditions for Iso-Octane, n-Heptane, Toluene and Gasoline Surrogate Fuels. SAE Technical Paper 2017-01-2190
40. Del Pecchia M, Breda S, d'Adamo A, Fontanesi S, et al. Development of Chemistry-Based Laminar Flame Speed Correlation for Part-Load SI Conditions and Validation in a GDI Research Engine. SAE Technical Paper 2018-01-0174
41. Sarathy S M, Vranckx S, Yasunaga K, Mehl M, Obwald P, Metcalfe W K, Westbrook C K, Pitz W J, Kohse K, et al. A comprehensive chemical kinetic combustion model for the four butanol isomers. Combustion and Flame 2012;159:2028–55
42. Inal F, Senkan S. Effects of equivalence ratio on species and soot concentrations in premixed n-heptane flames. Combustion and Flame 2002; 131:16-28.
43. Senda J, Fujimoto H, Multidimensional modelling of impinging sprays on the wall of Diesel engines, Applied Mechanical Review, 1999; 52:119-138
44. Senda J, Kanda T, Al Roub M, et al. Modeling spray impingement considering fuel film formation on the wall. SAE Technical paper 970047

6. Nomenclature

AFR	Air-to-Fuel Stoichiometric Ratio
CAD	Crank Angle Degree
CFD	Computational Fluid Dynamics
CO	Carbon monoxide
CoV	Coefficient Of Variation
DISI	Direct Injection Spark Ignition
EGR	Exhaust Gas Recirculation
EOI	End of Injection
ER	Equivalence Ratio
EVO/EVC	Exhaust Valve Opening/Closing
GDI	Gasoline Direct Injection
HC	Unburnt Hydrocarbons
IMEP	Indicated Mean Effective Pressure
IVO/IVC	Intake Valve Opening/Closing
LCE	Low-carbon Economy
LFS	Laminar Flame Speed
LFS_{spark}	Laminar Flame Speed in the Spark Plug Region
LUT	Look-Up Table
MFB	Mass Fraction Burnt
MON	Motor Octane Number
NDIR	Non-Dispersive Infra-Red
NOx	Nitrogen oxide
PAH	Polycyclic Aromatic Hydrocarbons

PFI	Port Fuel Injection
RANS	Reynolds Average Navier Stokes
RON	Research Octane Number
SI	Spark Ignition
SOI	Start of Injection
WOT	Wide Open Throttled

Appendix 1: Adopted sub-models and model constants (STAR-CD v4.28.033)

Models	Model Constants
Turbulence Model: k-ϵ RNG	<ul style="list-style-type: none"> All Default
Wall Heat Transfer Model: Grumo UniMoRE ^[26,27]	<ul style="list-style-type: none"> All Default Parameters Variable Prandtl Number Polynomial Conductivity
Combustion Model: ECFM 3Z SPARK ^[36]	<ul style="list-style-type: none"> $\alpha = 2.0$ $\beta = 1.0$ User defined Laminar Flame Speed^[17,39,40]
Ignition Model: Boudier ^[37] (FD ECFM)	<ul style="list-style-type: none"> Initial Kernel Radius: Fixed (2 mm) Spark duration: 2 ms
Fuel Injection: Lagrangian particles injection for each spray plume	<ul style="list-style-type: none"> 6 hole injector Full cone spray Injected mass flow rate from the experiments Hole diameter: 140 μm Cone Angle: 24° deg (for each spray plume) Injection temperature: 343 K Injection pressure: 100 bar
Droplet Primary Break-up: Rosin-Rammler distribution	<ul style="list-style-type: none"> Parameter X: 9e-6 m Parameter q: 8
Droplet Secondary Break-up: Reitz Model ^[30]	<ul style="list-style-type: none"> $We_{(Bag)} : 6$ $We_{(Strip)} : 0.5$ $Te_{(Bag)} : 3.1459$ $Te_{(Strip)} : 20$
Droplet-Wall Interaction: Senda ^[43,44]	<ul style="list-style-type: none"> Surface coefficient: 0.0154 BS: 1.0862 Wall friction coefficient: 0.7
Droplet Properties: Temperature dependent	<ul style="list-style-type: none"> Density, Surface tension, viscosity, specific heat, heat of vaporization, saturation pressure. Leidenfrost Temperature: Habchi^[35]
Numerics: MARS second order scheme	<ul style="list-style-type: none"> Momentum (U,V,W) Turbulence (k, ϵ) Temperature
Residual Tolerances	<ul style="list-style-type: none"> Momentum: 1e-3 Pressure: 1e-5 Temperature: 1e-12 Scalars: 1e-12
Numerical Time-steps	<ul style="list-style-type: none"> General: 0.05 CAD ($\approx 4.2\text{e-6s}$ @2000 rpm) During Injection, Combustion, Valves opening/closing: 0.02 CAD ($\approx 1.6\text{e-6s}$ @2000 rpm)

Appendix 2: Coefficients of LFS fitting polynomial

<i>n-butanol Coefficients</i>	<i>a</i>	<i>b</i>	<i>c</i>
<i>Nr.1</i>	55.350	1.889	-0.274
<i>Nr.2</i>	36.979	-0.005	-0.033
<i>Nr.3</i>	-240.544	9.167	-1.791
<i>Nr.4</i>	-316.128	13.175	-1.870
<i>Nr.5</i>	349.334	-14.165	3.502
<i>Nr.6</i>	573.816	-35.613	6.808

<i>Gasoline Coefficients</i>	<i>a</i>	<i>b</i>	<i>c</i>
<i>Nr.1</i>	41.922	1.774	-0.247
<i>Nr.2</i>	21.382	0.266	-0.148
<i>Nr.3</i>	-199.380	14.317	-2.864
<i>Nr.4</i>	-229.694	17.748	-2.690
<i>Nr.5</i>	326.096	-40.378	9.642
<i>Nr.6</i>	478.995	-64.969	13.932